B1-B2 transition in MgO shock compressed to 600 GPa

June K. Wicks[1], Saransh Singh[2], Marius Millot[2], Dayne E. Fratanduono[2], Federica Coppari[2], Martin G. Gorman[2], Zixuan Ye[1], Amy Lazicki[2], J. Ryan Rygg[4], Jon H. Eggert[2], Thomas S. Duffy[5], Raymond F. Smith[2],

Magnesium oxide (MgO) is a major component of the Earth's lower mantle and is expected to play a similar role in the mantles of large rocky exoplanets. Between 300-600 GPa, MgO transitions from the ambient NaCl B1 structure to a CsCl B2 structure with an expected large drop in viscosity, which may have profound implications for exoplanetary deep mantle dynamics. In this study, we constrain the phase diagram of MgO by conducting laser-compression experiments along the shock Hugoniot with in situ X-ray diffraction, velocimetry, and pyrometry to simultaneously determine crystal structure, density, pressure, and temperature. We identify the B1 to B2 phase transition at 400 GPa (around 9700 K), consistent with recent theory which accounts for the effects of phonon anharmonicity. The transformation is consistent with the Watanabe-Tokonami-Morimoto (WTM) mechanism. Our data are consistent with B2-liquid coexistence above 500 GPa and complete melting at 634 GPa. This study provides the first direct measurement of atomic-level changes in MgO under shock compression and represents the first determination of a phase transition mechanism under deep mantle pressures of super-Earth exoplanets.

INTRODUCTION

Magnesium oxide (MgO) is a major component of terrestrial planets and has long been a focus of high-pressure research [1, 2]. Found on the Earth's surface in small amounts as the mineral periclase, MgO forms a solid solution with FeO and comprises up to 17% of the lower mantle, which in turn accounts for more than half the mass and volume of the planet [3, 4]. As the third most abundant mineral in the lower mantle behind the stiffer perovskite-structured silicates (Mg,Fe)SiO_3 and $CaSiO_3$, MgO and its high pressure behavior plays an important role in controlling Earth formation and subsequent evolution.

MgO is studied as a model material for plastic deformation and dislocation mobility over a range of pressures thanks to its simple crystal structure, ionic bonding, and wide stability field [5]. Like many other binary compounds, MgO undergoes a reconstructive phase transition from the *NaCl* ($B1$-type, Fm$\bar{3}$m) to the *CsCl* ($B2$-type, Pm$\bar{3}$m) structure with applied/increasing pressure, recently reported between 363-580 GPa [6–8]; conditions expected in mantles of rocky exoplanets greater than about 5 Earth masses in size [9]. Empirical systematics and theoretical studies have emphasized the importance of this phase transformation on exoplanetary interior conditions due to an associated strong change in rheological properties with the high-pressure $B2$-phase exhibiting an estimated one hundred times reduction in viscosity [10, 11]. Recent theoretical work has found that this $B1-B2$ transition boundary (dT/dP) steepens at high temperatures, as anharmonic effects expand the stability of $B1$-MgO with respect to that of $B2$ [12–14]. Shock compression experiments are ideally suited to test these theoretical predictions as the Hugoniot crosses the $B1-B2$ phase boundary at high temperatures (> 8000 K, temperatures above which anharmonicity of $B1$ MgO is predicted to greatly increase [6, 8, 12–16]).

Previous indirect measures of this phase transition under shock compression present conflicting interpretations. Shock velocity measurements using electromagnetically-driven flyer plates attribute a density excursion on the shock Hugoniot to the $B1-B2$ phase transition at 363(6) GPa (where the number in parentheses denotes error in the last digit) [8]. Two independent decaying shock studies recorded large temperature excursions along the shock Hugoniot at pressures as low as ~400 GPa [6, 17], suggesting that the B1→B2 phase transition is accompanied by a surprisingly large change in enthalpy. Alternatively, this temperature signal may indicate $B1-$ MgO melting, a transition not inferred until higher pressures in velocity and reflectivity measurements (500−600 GPa) [6, 8, 18].

Here, we report on experiments which combine laser-driven shock compression with *in situ* X-ray diffraction in order to interrogate conflicting shock velocity, temperature, reflectivity, and ab initio measures of phase transitions along the MgO shock Hugoniot. This configuration allows us to simultaneously measure Hugoniot temperature, crystal structure and corresponding density at pressures of 400 to 634 GPa (temperatures of 9,000 K to 14,000 K), constraining the phase diagram of MgO near the $B1-B2-$*liquid* triple point.

RESULTS

Laser-driven shock compression was conducted on the Omega-EP and Omega-60 lasers at the University of Rochester's Laboratory for Laser Energetics. Twelve experiments were performed, increasing power of a shaped laser pulse on a polyimide ablator to generate shock pressures in the MgO sample ranging from 176→634 GPa. Shock-front velocity and reflectivity were monitored in a quartz window as a function of time using Doppler velocimetry (VISAR [19]), constraining peak stress in MgO samples during in situ X-ray diffraction measurements (XRD, [20]).

The two lowest pressure shots at 176 and 308 GPa were conducted on polycrystalline MgO. Higher pressure shots were conducted on single crystal MgO samples with the shock compression direction oriented along the [100] direction (similar to the previous shock experiments of Refs. [6, 8, 17]). The

Email address: wicks@jhu.edu (**June K. Wicks**)
[1]Dept. of Earth & Planetary Sciences, Div. of Mechanical Engineering; Johns Hopkins University, Baltimore, MD 21218, USA
[2]Lawrence Livermore National Laboratory, Livermore, CA 94550, USA
[3]Laboratory for Laser Energetics; University of Rochester, Rochester, NY, 14623, USA
[4]Dept. of Mechanical Engineering, Dept. of Physics and Astronomy; University of Rochester, Rochester, NY, 14623, USA
[5]Dept. of Geosciences; Princeton University, Princeton, NJ 08544, USA

initially-transparent single crystals provided access to determine shock-front temperature using streaked optical pyrometry (SOP, [21]), enabling experiments where pressure, temperature, and crystal structure were simultaneously measured.

Figure 1 shows these results in comparison to recent decaying shock experiments and theoretical calculations. The $B1 \rightarrow B2$ phase transformation begins between 397 and 425 GPa and 9,610-9,730 K, consistent with recent quasi-harmonic *ab initio* molecular dynamic calculations from Soubiran *et al.* [14]. The temperature of our $B1$-only data point (green circle in Fig. 1A) falls on the $B1$ Hugoniot, sampled in pyrometry of decaying shock experiments [6, 17]. Interestingly, temperature is constant between ~400-500 GPa, and X-ray diffraction intensity (Fig. 1B) indicates that the phase fraction of $B1$ versus $B2$ drops through that mixed-phase region.

Above ~500 GPa only the $B2$ phase is observed, where a drop in X-ray signal (including a loss of scattering from $B2$ (001) lattice planes by 520 GPa) may indicate partial melting, consistent with predictions from theoretical calculations [8, 13, 14]. The absence of X-ray signal at 634 GPa is consistent with complete melting, consistent in turn with shock transit [8], and shock front reflectivity measurements [6]. While low intensity diffuse X-ray scattering from the liquid is not detectable in these experiments, we infer partial melting from the drop in B2 X-ray signal, and draw a notional phase fraction in Fig. 1B.

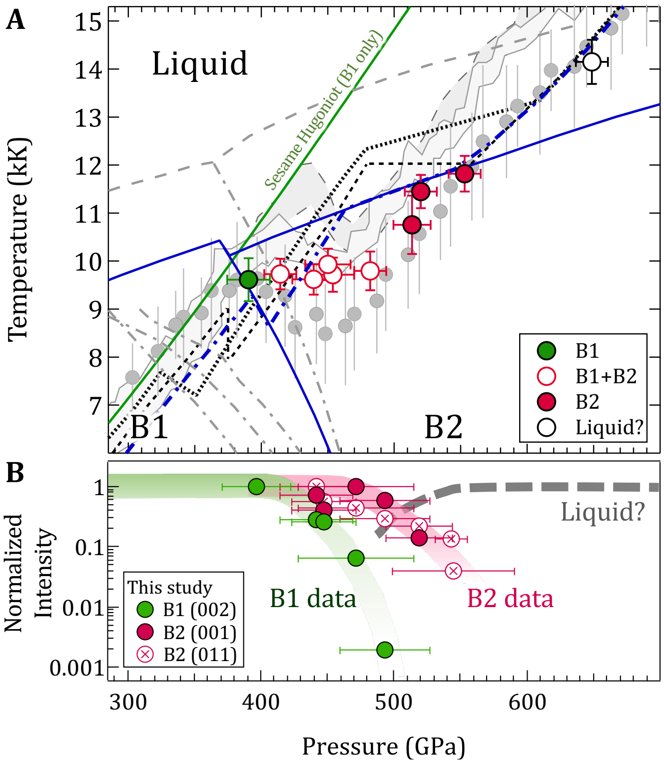

Figure 1. Summary of single crystal MgO results. (A) Measured temperature and phase identifications of MgO as a function of pressure (see also Fig. S1). The region of largest disagreement in previous shock experiments (gray bands, [17]; gray circles, [6] with a pressure correction from [8], see Fig. S11) is between 400 and 500 GPa, which corresponds in this study to that of the mixed B1+B2 phase region. In contrast, theoretical calculations predict smaller temperature excursions along the shock Hugoniot (dotted [8], black dashed [13], blue dash-dot [14]). The corresponding phase boundaries are shown for melting (gray dashed, [15]) and the B1-B2 boundary (gray dash-dot, in increasing pressure [16][22][23][15]). B1 and B2 temperatures measured in this study are most consistent with the phase diagram of recent theory (blue solid lines, [14]). The Hugoniot from the single phase (B1-only) Sesame EOS #7460 table is shown as the solid green curve [24]. **(B)** Integrated diffraction signal for B1 and B2 diffraction peaks as a function of sample pressure (see Materials and Methods). We note that the pressures associated with temperature (top, calculated over a skin depth at the shock front), differ slightly from those from XRD (bottom, calculated over the entire shocked volume). See Table S1, and Material and Methods for details.

Diffraction Texture Analysis Consistency with the WTM mechanism

Figure 2A (left) shows XRD data from a MgO [100] crystal shock compressed to a pressure (P) of 442(28) GPa. The data from five separate image plate detectors are combined and projected into 2θ-ϕ coordinates, where 2θ is the diffraction angle and ϕ is the azimuthal angle around the incident X-ray beam. In these coordinates, diffraction data project as straight lines of constant 2θ. Together with several lines from the Ta reference, we observed XRD signatures that can be unambiguously attributed to the B1 or B2 structure of MgO (see also Fig. 3).

The large single crystal spot at $\phi = 0°$ from the $(002)_{B1}$ lattice plane is consistent with a unimodal orientation distribution with a full width at half maxima ~8°, and centered around the initial starting orientation of the MgO single crystal. The high pressure B2 phase, on the other hand, is more richly textured, and depends on the phase transformation mechanism.

Theoretical calculations under hydrostatic compression [27] have identified two primary energetically favorable mechanisms for the B1-B2 transformation, the Buerger's mechanism [28] and the WTM mechanism [25]. The Buerger's mechanism describes compression along one of the <111>$_{B1}$ directions of the B1 unit cell and an expansion in the B1 orthogonal directions. A proposed modification of the Buerger's mechanism [27] – which introduces a monoclinic distortion to reduce the energy barriers – also produces the same B1-B2 orientation relationship. The WTM mechanism (originally proposed by Hyde and O'Keeffe [26]), is depicted in Fig. 2B, and requires a combination of two cooperative motions involving interlayer translation and intralayer rearrangement. Here, sliding of atoms within alternate $(001)_{B1}$ layers in the $[1\bar{1}0]_{B1}$ direction (Fig. 2B-left, blue arrows), is followed by an expansion in the $[110]_{B1}$ direction and contraction in all orthogonal directions (Fig. 2B-middle). This results in $(001)_{B1} \parallel (\bar{1}01)_{B2}$ and $[1\bar{1}0]_{B1} \parallel [010]_{B2}$ (Fig. 2B-right).

Using a forward diffraction model (see Materials and Method), we find that the Buerger's transition mechanism leads to a diffraction intensity distribution very different from the one measured in our experiments (see Fig. S9B). We therefore consider this mechanism is not active. On the other hand, the orientated B2-structure from the WTM mechanism does lead to an intensity distribution very similar to our measurements (Fig. 2B-right). All six orientation variants of the WTM mechanism were used for this simulation. Our findings are in agreement with the recent observation of the WTM mechanism for the low-pressure (~2 GPa) B1→B2 transition in in KCl under shock compression [29]. The texture analysis indicates that the compressed B1 phase is still highly textured at up

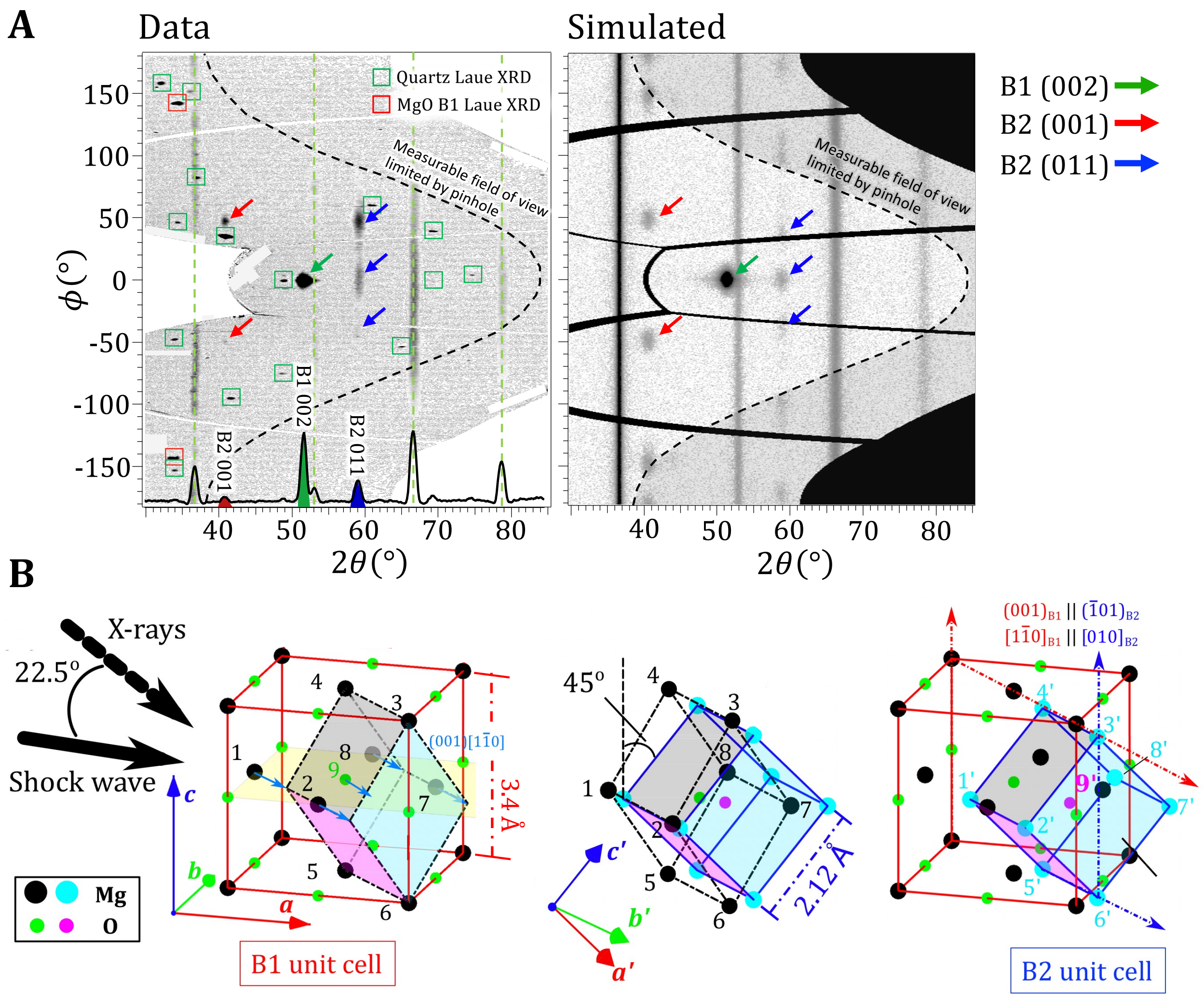

Figure 2. Texture analysis of X-ray diffraction data. (A) Qualitative agreement between experimental image plates projected in 2θ-ϕ and a simulated diffraction pattern at P = 442(28) GPa. (Left, bottom axis) An averaged intensity lineout shows features consistent with both the B1 and B2 phases, and Ta calibrant at 1 bar. The red and green boxes represent simulated Laue diffraction locations from MgO B1 and uncompressed quartz [001] single crystals, respectively, from broadband X-ray thermal emission generated within the Cu He-α X-ray source plasma (see Materials and Methods). Also shown are Ta reference peaks (dashed green lines). **(B)** Our data is consistent with the WTM mechanism [25, 26] which is described in two steps: (left) sliding of atoms within alternate $(001)_{B1}$ layers in the $[1\bar{1}0]_{B1}$ direction (blue arrows along yellow plane) to unit cell denoted by black dashed-dot lines, followed by, (center) an expansion in the $[110]_{B1}$ direction (vectors connecting atoms 1-8, 2-7) and a uniform compression perpendicular to this direction, i.e., the $[001]_{B1}$ and the $[1\bar{1}0]_{B1}$ direction (atoms 3-6, 4-5, 1-2, 8-7). The resulting $[010]_{B2}$ axis is orientated 45° to $[001]_{B1}$. (right) The WTM mechanism results in $(001)_{B1} \parallel (\bar{1}01)_{B2}$ and $[1\bar{1}0]_{B1} \parallel [010]_{B2}$ and produces six variants which can be detected in our experiments.

to 500 GPa (V/V_0=2) and 10,000K (0.9 eV), and transformation into the B2 phase is consistent with a Watanabe-Tokonami-Morimoto (WTM) pathway. These measurements up to 634 GPa and 14,150 K provide the first direct lattice-level confirmation of the B1→B2 phase transformation on the Hugoniot, and the first thermodynamic constraint of the transformation along any compression path.

We also considered the possibility of fiber texture and/or the Buerger's mechanism [28] for the B1→B2 phase transition. However, any other combination of the transformation mechanism and sample texture were in poor agreement with our measurements leading us to conclude that the texture of the B1 as well as the B2 phase is a unimodal orientation distribution, and the WTM mechanism is active during the B1→B2 phase transition in [100] compressed MgO.

XRD determined density

X-ray diffraction results of shock compression experiments are summarized in Fig. 3, plotted in comparison to predictions from both the 0-K isotherm and high temperature Hugoniot data. In Fig. 3A, d-spacing as a function of shock pressure is plotted for the $(002)_{B1}$ (green circles), $(001)_{B2}$ and $(011)_{B2}$ (maroon circles). P_{MgO} is calculated from shock velocity measurements (see Fig. 6 and Materials and Methods).

Comparable experimental constraints are made under static compression using diamond anvil cells [30], and low temperature ramped compression using laser drives, which identified the B1-B2 transition at 600 GPa [7]. Our identification of B2 at 425 GPa, along the high temperature Hugoniot, confirms that the B1-B2 transition has a negative Clapeyron slope.

Calculated P_{MgO} is plotted against MgO density, ρ_{MgO}, in

Fig. 3B. Here, density is calculated from the d-spacing values in Fig. 3A, with the B2 data (maroon circles) an average from the $(001)_{B2}$ and $(011)_{B2}$ values. The diffraction data for all shots are shown in Fig. S4B along with integrated lineouts of d-spacing (Fig. S4C). ρ_{MgO} for each shot is listed in Table S1A. Based on linear extrapolation of U_S - u_P data below 363 GPa we estimate the volume change of our X-ray diffraction data due to the B1-B2 phase transformation is 8.6 ± 2.5 %, which is higher than expected from theory (~5.5%) [8].

Optical Skin depth of shock-compressed MgO

The target design in our experiments is shown in Fig. 4A, and consists of a polyimide ablator, 0.5-μm thick Al directly coated onto a 80-μm thick MgO [100] crystal, and 50-μm quartz (see Materials and Methods). The temperature at the shock front during shock transit within the initially transparent MgO and quartz layers is measured with the Omega-EP streaked optical pyrometer (SOP) [21]. The SOP records thermal emission integrated over a 590 to 850-nm spectral range, with 1D spatial resolution over the 300-μm field of view (Fig. 4B and Materials and Methods).

Our pyrometry data allows us to constrain the optical skin-depth of shock-compressed MgO. This describes the thickness of shocked material behind the shock front from which optical photons are emitted and contribute to the recorded SOP signal (1/e of the surface value). As the temporally steady shock propagates through the target assembly (Fig. 4A) with a shock velocity, U_S, the Al/MgO layer interface moves with a particle velocity, u_P. Thermal emission from the hot, compressed Al layer, which is constant over the lifetime of the experiment, is transmitted and attenuated through the shocked-MgO crystal and recorded by the SOP. The raw SOP data for four different pressures are shown in Fig. 4B. The calculated optical-depth (Fig. 4C) is determined by considering the time taken for the recorded Al thermal emission to drop from a peak level to 37% of the peak, while calculating the shock-thickness over this period from estimates of U_S and u_P. The corrected SOP traces exhibit a clear Beer-Lambert behavior and exponential fits yield values for optical depth d = $1/\alpha$, where α is the absorption coefficient (see inset to Fig. 4C). Our data shows a pressure-dependent optical skin-depth of 12→<1μm (397→634 GPa), as described by the functional form,

$$d = 0.5 + 11.215e^{\frac{-P-397}{35.788}}, \tag{1}$$

where the optical depth d is in μm and the pressure, P, is in GPa. Measurement uncertainties account for the variation of thermal emission in time over the 300-μm SOP field-of-view.

DISCUSSION

Our study presents two significant findings. The first is that the observed pressure range of the B1-B2 coexistence region spans from 400 to 500 GPa, a transition width of 100 GPa. This large pressure coexistence width is not predicted in any of the theoretical constructions of the MgO phase diagram (Figs. 1 and S1). The second is the constant temperature observed throughout the B1-B2 phase transition. This raises the question of whether both the B1 and B2 phases maintain the same temperature or if it is the average system temperature that remains constant. The temperature consistency suggests a possible thermodynamic equilibrium or energy redistribution during the phase transition.

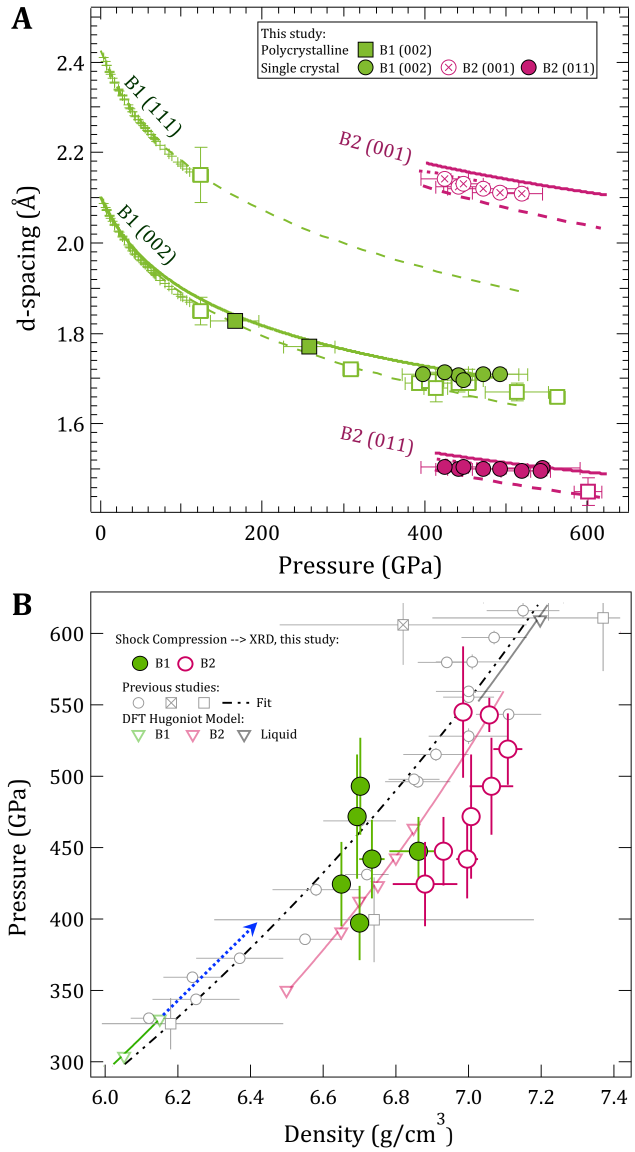

Figure 3. Lattice spacings of observed diffraction peaks of MgO and determined density. (A) d-spacing as a function of pressure for our data (maroon and green circles) are compared to those measured under ramp compression (open squares, [7]). Static data are shown as crosses with an extrapolation to high pressure using a Vinet EOS fit (green dashed) [30]. Theoretical d-spacing curves for the B2 phase are shown for calculations both at 0-K [16] (maroon dashed), and along the Hugoniot (maroon dotted) [8]. d-spacing determined from a cubic fit to Hugoniot shock and particle velocity data is also plotted (solid green and solid maroon curves) [8]. **(B)** Calculated pressure and measured density for the B1 (green circles) and B2-phase (maroon circles). Hugoniot data based on shock-speed measurements are shown as the open circle, crossed circle, open square and crossed square symbols [2, 6, 8, 31–34]. A Hugoniot based on DFT calculations is shown as the green (B1), maroon (B2) and black (liquid) open triangles [8]. Solid line fits to these points are based on linear fits in U_s-u_p. The blue dashed arrow represents an extension of the B1 phase up to pressure where we see only B1 in our XRD data. An expanded pressure-density plot range is shown in Fig. S2.

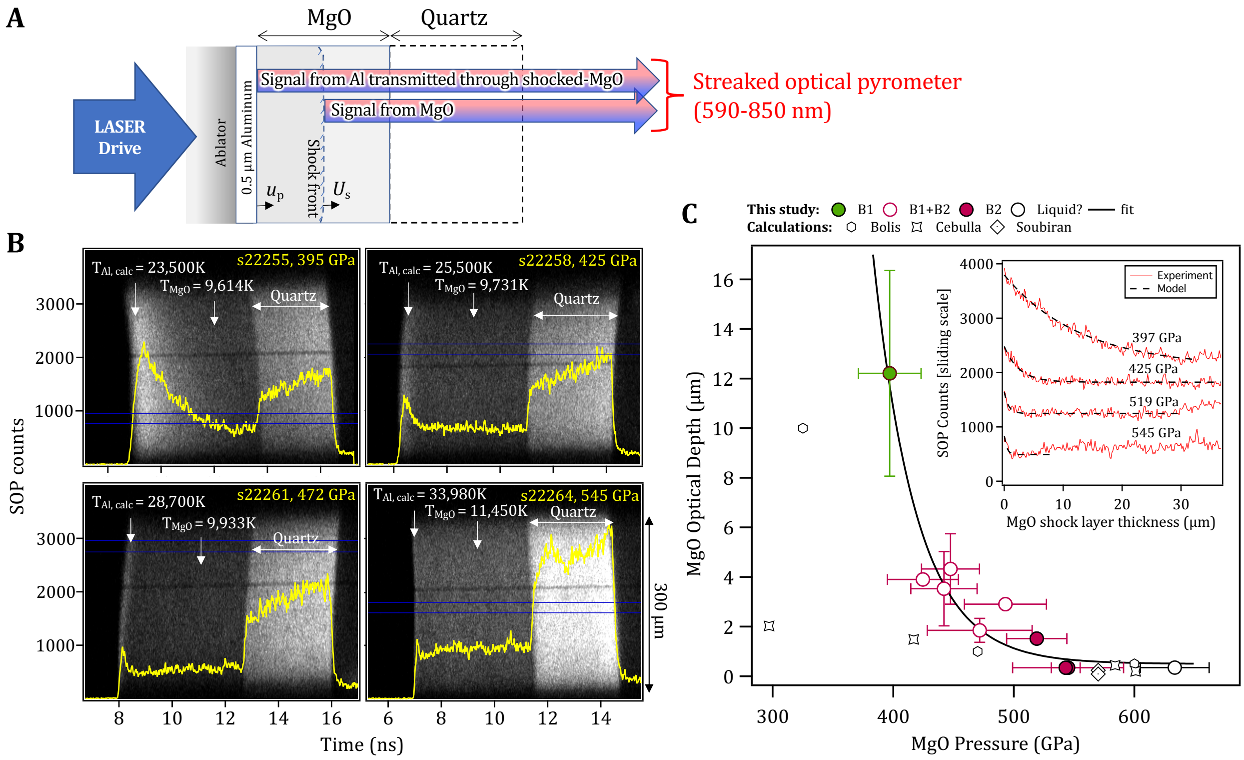

Figure 4. Measurement of optical depth in shocked MgO as a function of pressure. **(A)** The target design consists of a polyimide ablator, a 0.5 μm Al layer directly coated on to a 80 μm thick MgO [100] single crystal, and a 60 μm thick quartz layer. As the shock propagates through the target assembly, thermal emission from the hot, compressed Al layer, ~constant over the lifetime of the experiment, is transmitted and attenuated through the shocked-MgO crystal and recorded by the SOP diagnostic. The raw data from the SOP for four different pressures is shown in **(B)** with intensity lineouts, taken from region defined by two horizontal blue lines, shown as the bold yellow curves. In each case the calculated Al shock temperature is shown [35] as well as the measured MgO shock temperature. **(C)** (Inset) The optical depth is determined by considering the time taken for Al thermal emission to drop from a peak level to 37% of the peak, while the associated MgO shock-thickness is calculated from U_S and u_P estimates. (Main plot) Estimated values of optical depth are plotted along with calculations based on theory [13, 17, 36] (see Materials and Methods).

P-T-ρ Hugoniot conditions for B1-B2 transition compared with previous studies

Our study provides the first direct experimental constraints on phase relations and structures in the MgO system along the Hugoniot. We observe the B1-only phase up to 397(26) GPa and 9614(450) K. XRD peaks associated with B2 phase are observed at 425(30) GPa and 9731(320) K. These data are in excellent agreement with the recently quasi-harmonic *ab initio* calculations of the Hugoniot transition pressures of Soubiran *et al.* (2018, 2020) [13, 14] (dashed-dotted blue curve in Fig. 1A). Our measured B1-B2 P-T onset values are significantly higher than earlier theoretical estimates along the Hugoniot (325 GPa [8]). A full summary of published theoretical predictions compared with our data is shown in Fig. S1. Our B2 onset pressure is also higher than the 363(6) GPa inferred from recent shock and particle velocity measurements [8].

In our experimental geometry measurements the $(002)_{B1}$ reflection provides a constraint of density in the direction perpendicular to the shock propagation direction. In this uniaxial compression geometry, and in the presence of deviatoric stresses (not constrained here), the compressibility (density) in this direction would be less than the compressibility along the shock propagation direction, as accessed by experiments which constrain the Hugoniot through U_S-u_P measurements [8]. Given that, the high density of the B1-only point at 397 GPa relative to U_S-u_P data, and DFT calculations is an intriguing observation (Fig. 3B). This could potentially serve as evidence of phonon anharmonicity. Anharmonicity in MgO is predicted to reduce both thermal expansion with increasing pressure, and bulk modulus with increasing temperature [37]. In both cases this would serve to increase compressibility. In addition, theoretical studies on MgO show evidence of C44 elastic constant softening within the B1 and B2 phases at pressures approaching the phase transition [38].

Effect of optical depth on temperature determination

Figure 4C shows the experimentally-determined optical skin depth as a function of shock pressure. For the SOP determination of shock temperature (Fig. 1A), thermal emission is collected from an extended volume which encompasses the shock front and pressure states behind the shock front. This volume is defined by the optical depth. The values reported in Fig. 4C are significantly higher than values assumed in shock decay studies of MgO [6, 17]. For example, in the study of McWilliams *et al.* [6] the optical depth of shocked-MgO was taken as ~1-μm (or negligible) for pressures above 300 GPa. For those experi-

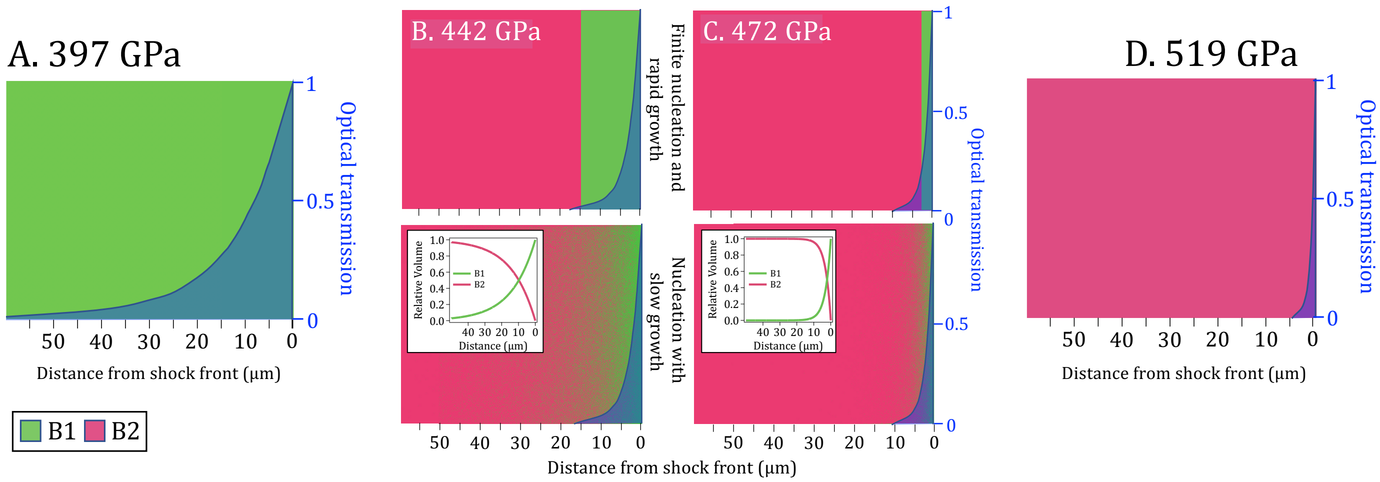

Figure 5. Possible distributions of phase fractions within compressed MgO. (A) Representation of compressed volume of MgO at a shock pressure of 397 GPa (B1-only, green). Based on the measured optical depth at this pressure (~12 μm, Fig. 4C) the optical transmission as a function of distance away from the shock front can be calculated (blue shaded region). This represents the relative volume-dependent contribution to the SOP temperature measurement (as plotted in Fig. 1A). The representation in **(D)**, for a shock pressure of 519 GPa is B2-only (maroon) with a measured optical depth of < 1 μm (Fig. 4C). **(B)** and **(C)** represent pressures within the XRD-measured mixed B1+B2 phase region (Fig. 1A). For each pressure the relative proportion of B1 (green) and B2 (maroon) phases are estimated by relative changes in normalized XRD-intensity with pressure, as plotted in Fig. 1B. As our XRD-data is volume-integrated, we cannot determine how the B1 and B2 phases are distributed within the compressed MgO, and knowledge of this distribution within the optical skin depth is needed to correctly interpret the measurements of temperature. Here we consider two possibilities based on different transformation kinetics models: (upper) finite nucleation and rapid (instantaneous) growth into the B2 phase, which results in a two-phase structure with distinctly separated B1 and B2 volumes, and (lower) nucleation with slow growth, resulting in a random mixed phase assemblage within the measured optical skin depth. Our data is most consistent with the this latter model and B2 nucleation time scales of < 0.25 ns.

ments, and due to strong pressure and temperature gradients behind the shock front, a large optical depth in the B1-phase, will give rise to an overestimation of shock front temperature [6], which will diminish as a function of increasing pressure. A detailed correction of previously reported shock decay data based on the optical depth values in Fig. 4C is beyond the scope of this paper.

In temporally steady shock compression experiments, as reported here, there are minimal pressure gradients behind the shock front and the determination of temperature is unaffected by a pressure-dependent optical depth as long as the shocked thickness exceeds the optical depth, e.g., Fig. 5A, D. However, as discussed below, and illustrated in Fig. 5B and C, complications in interpreting SOP data arise for mixed phase volumes.

Mixed B1-B2 phase region in Fig. 1A

The observed shock temperature of the mixed B1+B2 phase region in Fig. 1A remains constant from ~420-490 GPa. This pressure range is several times larger than equilibrium calculations of mixed phase along the B1-B2 phase boundary (Fig. S1). As illustrated in Fig. 5B and C, the interpretation of the SOP determination of temperature in this region is complicated by the presence of the mixed phase – where the B1 and B2 phases may exist at different temperatures – and is further affected by the potential distribution of the phases within the sampled volume behind the shock front, i.e., the volume defined by the pressure-dependent optical depth.

X-ray diffraction, provides volume-integrated structural information, and therefore can not distinguish between distinctly separated B1 and B2 volumes (Fig. 5B-, C-upper), or a mixed phase assemblage (Fig. 5B-, C-lower). The SOP, on the other hand, integrates signal over a skin depth behind the shock front, measured to be around 4 μm at 442 GPa (blue shaded region in Fig. 5C). Observation of a constant temperature in the mixed phase region, rather than a continual increase with pressure along the B1 Hugoniot (green curve in Fig. 1A), indicates that the SOP samples both the B1 and B2 phases, and is therefore consistent with the existence of a mixed phase assemblage within the optical skin depth. Considering a shock velocity of 16.3 µm/ns at 442 GPa [8], this places a upper limit of ~0.25 ns on nucleation into the B2 phase at this pressure.

As observed in other phase-transforming materials [39, 40], the time required for nucleation and growth into the new phase is inversely proportional to the level of shock overpressurization from the equilibrium transformation pressure [39]. Therefore, with increasing pressure, the B1 fraction within a shocked volume is expected to diminish (as observed in Fig. 1B).

The highest pressure we observe *only* compressed B1 is 397(26) GPa. The shock transit time through the MgO sample at the time of X-ray exposure was ~3.25 ns. We note, that this pressure may lie within the B2 stability field *if* the transformation time into the B2 phase is slower than this shock transit time.

CONCLUSIONS

By measuring crystal structure and temperature as a function of pressure, our experiments uniquely bridge previous measurements of propagating shock fronts, which constrained density and temperature via shock front velocity and pyrometry, respectively [6, 8, 17]. X-ray illumination over 2 ns integrates over tens of microns behind the shock front, accessing different timescales than those probed in shock front measurements.

We first observe the presence of the high-pressure B2 phase at 425(30) GPa, confirming most recent theoretical predictions of a transition boundary just below that on the shock Hugoniot [13, 14]. B1+B2 co-existence is observed from 425(30)-493(34) GPa, a wide mixed phase region reflecting a volume-driven phase transition, as predicted by theory [8].

Using a forward diffraction model, we show that the measured orientation relations of observed X-ray diffraction signal is consistent with a Watanabe-Tokonami-Morimoto transformation mechanism. This is in agreement with transition-path-sampling molecular-dynamics simulations [41, 42] and low-pressure measurements on KCl [29]. This mechanism is in contrast to the modified Burger's pathway, which is suggested to be favored for the B1-B2 transition of CaO [43].

From 519(25)-545(46) GPa (~10700-11450 K), only B2 diffraction peaks are observed. The progressive decrease of B2 diffraction signal over this range is consistent with B2-liquid co-existence in agreement with previous predictions along the Hugoniot [8]. Our interpretation of full melt at 634(29) GPa is also consistent with those studies. Future work is needed to provide experimental constraints on the B1-B2 Clapeyron slope and to determine how compression timescale and crystal orientation affect the determined B2 onset pressure.

MATERIALS AND METHODS

Sample preparation, PXRDIP experiments

The target design for experiments on Omega-EP is shown in Fig. 4A and consists of a 125-μm thick polyimide ($C_{22}H_{10}N_2O_5$) ablator, 75-μm thick single-crystal MgO [100], and 50-μm thick z-cut single-crystal quartz (α-SiO_2), held together with ~1-μm-thick glue bonds. The high-purity MgO single crystals (> 99.95% purity, <100>±0.5°, density 3.58 g/cm^3) were supplied by MTI corporation. Typical impurities are <50 ppm. A 0.5-μm thick Al layer was deposited directly onto the MgO crystal to enhance reflectivity for velocimetry measurements, and an anti-reflection (AR) coating was applied to the quartz free-surface to suppress photon back reflection at quartz/vacuum interface. The target design for a subset of shots on the Omega-60 laser on polycrystalline MgO (99.5% purity, further described in Ref. [44]), consists of a 100-μm thick polyimide layer, 50-μm thick polycrystalline MgO and a 50-μm thick quartz layer.

Laser Configuration.

On Omega-EP, a 10-ns 351-nm laser pulse was focused to a 1.1-mm diameter spot on the polyimide front surface. For the experiments on Omega-60, a ~7.4-ns composite pulse shape was built with two 3.7-ns laser pulses, focused to a 0.8-mm diameter spot. Spatial smoothing of the focal spot intensities was achieved with distributed phase plates inserted into the beamlines. In both cases laser ablation resulted in uniaxial compression of the target assembly in a near temporally-steady shock. By varying the laser intensity the pressure in the MgO sample was systematically increased from 176 to 634 GPa. In total, 12 shots were performed (10× [100] single crystal (Omega-EP), 2× polycrystalline (Omega-60)) (see Fig. S3).

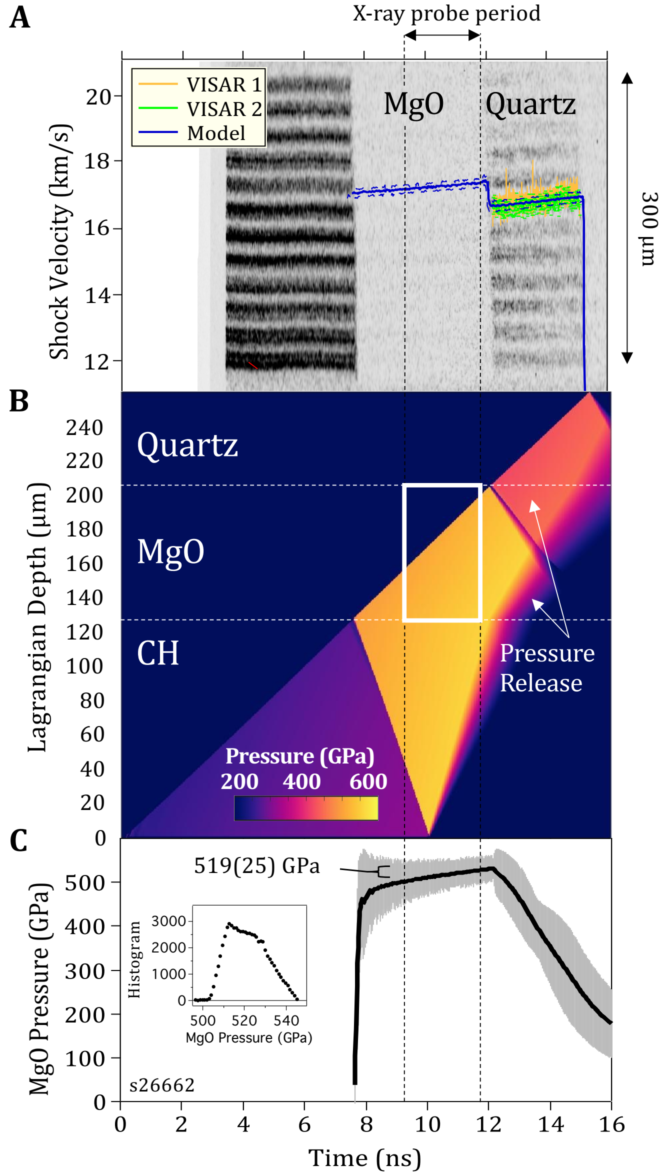

Figure 6. Pressure determination of shock compressed MgO. (A) Raw VISAR image with shock transit periods within the MgO and quartz layers highlighted. Shock velocity in quartz, $U_{S,Qtz}$(t), measured by two independent VISAR channels, is shown with uncertainties as the orange and green traces. Simulated U_S(t) though the MgO and quartz layers is shown as the blue trace, with dashed blue error bands based on experimental measurement uncertainties. Time = 0 ns represents the laser turn on time. **(B)** P(x,t) output from a HYADES hydrocode simulation [45]. **(C)** Calculated average pressure versus time within the MgO sample with uncertainties which reflect the pressure distribution during the x-ray probe period. Inset figure shows a histogram of the pressure states within the MgO sample during the x-ray probe time (white box in **(B)**). See Materials and Methods for details.

X-ray Diffraction Measurements

Laser-generated Cu plasmas illuminated the shocked MgO with quasi-monochromatic X-rays (8.37 keV, 1.48 Å) for 2 ns [46]. Diffracted X-rays, collimated by a Ta pinhole positioned directly behind the target to an incidence angle of 22.5° to target normal, are recorded in transmission geometry on image

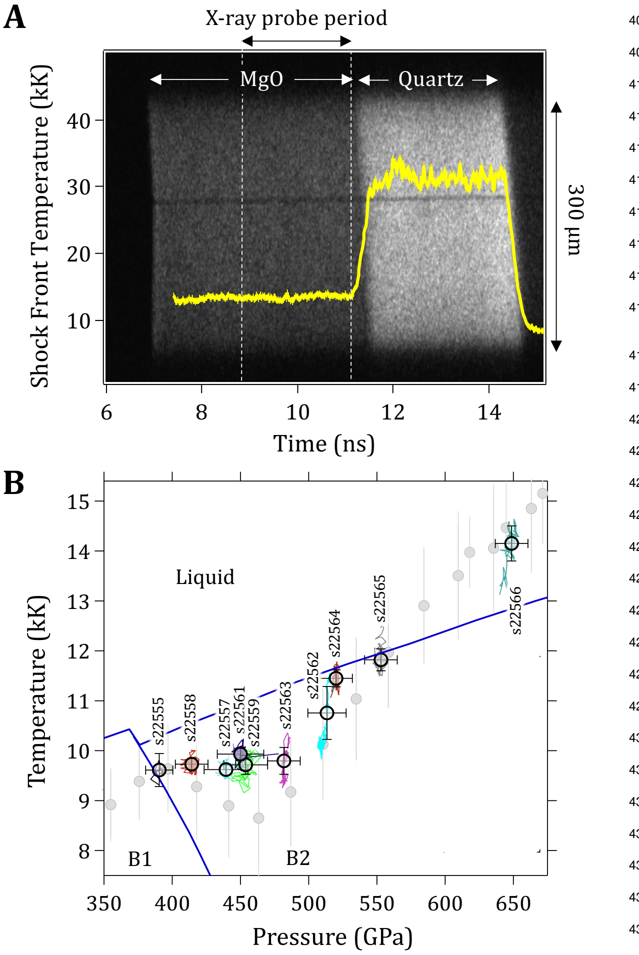

Figure 7. Determination of MgO temperature from pyrometry measurements. **(A)** Raw streaked optical pyrometry (SOP) data for shot s22264 (P = 520(12) GPa), where thermal emission from the MgO and quartz layers, over the 300 μm field of view, are indicated. Also plotted is the calculated shock front temperature (yellow, see Materials and Methods). **(B)** Measured MgO shock-front temperature plotted as a function of calculated MgO shock-front pressure during the X-ray probe period. The shot number for each data point is shown. Recent quasi anharmonic calculations by Soubiran *et al.* (2020) for the melt, and the B1-B2 phase boundary (blue curves) are also shown [14]. The gray circles represent decaying shock measurements by McWilliams *et al.* [6] which have been corrected in pressure based on the subsequent U_s-u_p measurements by Root *et al.* [8] (see Fig. S11). Data points (as plotted in Fig. 1A) are shown as circles with uncertainties which represent the standard deviation of the measured temperature and calculted pressure distribution (colored curves) during the probe period. An additional estimated ± 300 K systematic temperature uncertainty associated with SOP measurements is combined with the distribution error bars shown here, for the uncertainties shown in Fig. 1A (see Materials and Methods).

plate detectors [20]. Diffraction peaks from the uncompressed Ta pinhole are used to accurately determine the experimental geometry, i.e., the position of the X-ray source and scattering center within the sample, with respect to the various image plate detector panels. We also preform 2D Statistics-sensitive Non-linear Iterative Peak-clipping (SNIP) background subtraction and angular dependent corrections as in Refs [20, 47]. The image plate planes are projected into 2θ (diffraction angle) - ϕ (azimuthal angle) space in Fig. 2A, or in ϕ - d-spacing coordinates as shown in Fig. S4B.

Normalized diffraction intensity from Fig. 1B:
The shot-to-shot diffraction intensity is normalized by accounting for variations in the X-ray source flux, and any variations in the compressed sample volume. The former is constrained by considering the intensity of the uncompressed Ta pinhole peaks, and the later is determined from the VISAR record. In addition a background subtraction is performed by subtracting the signal from adjacent regions on the image plates where no crystalline diffraction is observed.

Forward Model For X-ray Diffraction Texture Analysis

Forward diffraction simulations were performed to predict the expected signal for an arbitrary crystal orientation distribution (e.g., Figs. 2A and S9B). Given all experiment parameters, the model computes the expected intensity distribution in $2\theta - \phi$ space. The parameters include the crystal structure, lattice parameters, phase fractions and crystallographic texture of compressed and high-pressure phases. The texture information is used to modulate the powder diffraction intensity in the azimuthal direction. In addition to the material related parameters, the model also takes the peak shape functions as inputs. These parameters can be used to specify the instrumental broadening, microstrain and grain size effects. The crystallographic texture is represented using a finite element representation of the Rodrigues space fundamental zone [48–50]. The forward model calculation is done in two steps: (i) the powder diffraction intensity for the B1 phase, B2 phase and Ta pinhole is calculated as a function of 2θ. Since this is a powder diffraction calculation, the intensity along the ϕ dimension remains constant. (ii) The assumed unimodal orientation distribution function for the starting B1 phase and the predicted B2 phase orientation from WTM/Buerger's mechanism is projected as pole figures (Figs. S6, S7, S8). This gives us the intensity variation along the azimuth for the B1 and B2 phase, which is multiplied with the powder intensity distribution from step (i). The area masked by the pinhole is superimposed on the intensity distribution obtained from these calculations. Note that the absorption due to varying X-ray path length after diffraction is not accounted for.

Consistency with the WTM mechanism: To test consistency with previously reported values of stretches required in the phase transition, our XRD-determined lattice parameters were used to compute the principal stretches (i.e. expansions/contractions) for both mechanisms. The stretches for both mechanisms are reasonable and only differ by a few percent from previously reported values for NaCl [51] (see sections S1,S2 and Fig. S10). However, using the forward diffraction model, we find that the Buerger's transition mechanism leads to a diffraction intensity distribution very different from the one measured in our experiments (see Fig. S9). We therefore consider this mechanism is not active. On the other hand, the orientation relationship predicted by the WTM mechanism leads to diffraction signal reflections consistent with our data (Fig. 2A). .

Mosaic Spread: To get good qualitative agreement with our XRD data (Fig. 2A) we find that it is necessary to introduce a level of mosaic spread to the B1 and B2 phases (∼ 8° and 10° respectively). This is akin to using a unimodal orientation distribution function for both the phases. The mosaic spread is a measure of the orientational order of the crystallites comprising the bulk material: the smaller the mosaic spread, the greater the orientational order of the sample [52, 53]. The mosaic spread is defined as full width at half maximum of the orientation distribution function. The larger the mosaic spread the greater the crystal rocking curve and the more likely Bragg diffraction conditions are met. The orientation of compressed B1 phase centered around the orientation of the ambient B1 phase, whereas the orientation of the B2 phase is centered around the six orientation generated by the WTM mechanism.

Shock Velocity Measurements

Shock velocity is measured using a line-imaging VISAR (Velocity Interferometer System for Any Reflector) with two independent channels set with different velocity sensitivities (4.3697 or 7.8167, and 3.1903 km/s per fringe shift for VISAR channels 1 and 2, respectively) to provide independent measurements of velocity and resolve any ambiguities associated with sharp jumps that exceed the time response of the system [54]. We use standard ambient pressure values for c-cut quartz (α-SiO_2): ρ_0 = 2.648 g/cm^3, and a refractive index at the 532-nm VISAR wavelength of 1.547. A representative VISAR interferogram, which encodes velocity information as fringe shifts, is shown in Fig. 6A.

At early times, the 532-nm VISAR probe beam reflects off a 0.5-μm thick Al layer which is coated directly onto the MgO surface facing the polyimide. As the shock enters the 75-μm thick MgO layer (at ∼7.8-ns), the target reflectivity dissipates (no fringes) due to the combined effects of shocked-region opaqueness, non-reflectivity of the shock front [6, 17], and a loss in aluminum reflectivity as a function of shock temperature [55]. After transit through MgO, the shock enters the 50-μm thick quartz layer (∼12 ns). For shock states greater than 100 GPa, shocks in quartz are reflective and under these conditions VISAR records quartz shock velocities directly [56]. $U_{S,Qtz}(t)$ is measured with the two VISAR channels (orange and green curves with 1σ uncertainties). Each velocity measurement is determined from the average and standard deviation over a 300-μm field-of-view, which captures any increased velocity distribution due to spatial non-planarities within the drive (e.g. shock-front tilt due to gradients in the glue layer thickness). In addition, we use a conservative estimate in velocity uncertainty based on an assumed 5% accuracy in determining fringe phase shift. A summary of the laser pulse shapes used, and the associated measured U_S (t) traces for all shots are shown in Fig. S3.

Pressure Determination

Over the pressure range of our study, the shock front in MgO is not highly reflective [6], while the shock front in quartz exhibits metallic-like reflectivity [57]. Using VISAR we measure the MgO shock entry and exit times, and the quartz shock velocity $U_{S,Qtz}$(t). The pressure history in MgO is determined by simulating the experimental conditions with a 1D hydrocode, HYADES [45], which calculates the hydrodynamic flow of pressure waves through the target assembly in time (t) and space (x) (Fig. 6B). The inputs to the hydrocode are the thicknesses of each of the constituent layers of the target, including the measured epoxy layer thicknesses (∼1-3-μm), an equation-of-state (EOS) description of each of the materials within the target, and laser intensity as a function of time, $I_{Laser}(t)$. We find that pressure (GPa) in the polyimide ablator scales as 4.65×$I_{Laser}{}^{0.8}$, with $I_{Laser}(t)$ (PW/m^2) calculated from measurements of laser power (Fig. S3A) divided by an estimate of the laser spot size. The latter is not well defined however and so a scaling factor is applied to $I_{Laser}(t)$ to obtain improved agreement with the experimental observables.

A series of forward calculations were run with iterative adjustments of $I_{Laser}(t)$ (few % level) until convergence was reached between the calculated $U_{S,Qtz}(t)$ and the average of the measured $U_{S,Qtz}$(t) curves (solid blue curve in Fig. 6A). Once achieved, the calculated $P(x,t)$ (Fig. 6B), was used to determine P_{MgO}±$P_{Distribution}$ during the x-ray probe period (white box in Fig. 6B), from the pressure distribution histogram peak (P_{MgO}) and full-width at half maximum ($P_{Distribution}$) (e.g., inset to Fig. 6C). The steps described above were repeated to match the bounds of $U_{S,Qtz}(t)$ experimental uncertainty (dashed blue curves in Fig. 6B). In this way the final determined calculation of P_{MgO}±$P_{Distribution}$ was directly related to the experimental uncertainties. This method of pressure determination explicitly accounts for any temporal non-steadiness in the compression wave. The HYADES fits to the experimentally determined $U_{S,Qtz}$(t) curves for all shots is shown in Fig. S3B. Our experimental geometry also permits temporal measurements of MgO shock entry and exit times, which permits calculation of average U_s, but does not capture deviations in U_s due to non-steadiness of the drive. Nevertheless, these transit time U_s values gave sample pressures [8] in general consistency with the approach outlined above.

We note that the XRD determination of structure is volume-integrated, whereas the temperature is measured over an optical skin depth at the shock front. Therefore the pressure associated with XRD and T measurements are calculated accordingly (as reported in Table S1). For this reason the pressures for the data in Fig. 1A and 1B are slightly different.

In our experiments, the sample is uniaxially-compressed. While the use of the term "pressure" throughout the paper suggests a hydrostatically-compressed state, we cannot rule out the presence of deviatoric stresses which would, in the case of our measurements, and all previous Hugoniot measurements [2, 6, 8, 31–34], give rise to higher values of longitudinal stress and therefore reported pressure. In the analysis of Fowles [58] using the Lévy - von Mises yield criterion [59] this stress deviation corresponds to two-thirds the yield strength. However the high pressure strength of MgO is unknown.

Equation-of-state tables: The EOS tables used in the hydrocode simulations for MgO (Sesame #7460) and quartz (Sesame #90010) describe Hugoniot pressure–particle velocity paths as shown in Fig. S5A [24]. Also plotted are Hugoniot data for MgO [6, 8, 32, 33], and quartz [60]. Pressure residuals between measured Hugoniot data and the calculated Hugoniots are shown in Fig. S5B. While Sesame #7460 is in good agreement with previous data on MgO, there is an average systematic offset of 1.6 ± 1.9 GPa between the quartz Hugoniot data and the quartz EOS table used in the pressure determination calculation, over the pressure range of our study. This level of disagreement produces a systematic offset in the calculated MgO pressure but at a level much less that other contributors to pressure uncertainty, e.g., the pressure distribution within the sample due to temporal non-steadiness of the shock drive (Fig. 6C). Uncertainty in pressure: The MgO EOS used for pressure determination does not describe the expected ∼5% volume collapse associated with the B1→B2 phase transformation. This will introduce a systematic offset in the determined pressure for pressures above the B2-phase onset. However, this offset is expected to be small relative to the calculated pressure distribution and is thus neglected. Additional contributions to pressure uncertainty that are small relative to the calculated pressure distribution are uncertainties in laser beam timing (50-ps), VISAR timing (50-ps), sample thicknesses (1-μm), quartz refractive index uncertainty, and the deviations between the hydrocode-calculated $U_{S,Qtz}(t)$ and the experimentally-determined $U_{S,Qtz}(t)$ (Fig. 6A). Calculated $P_{MgO} \pm P_{Distribution}$ for all shots are listed in Table S1A.

Optical Skin Depth

In Fig. 4C, the experimentally determined optical skin depth as a function of shock pressure is shown. These values are determined by considering the time taken for the recorded Al thermal emission to drop from a peak level to 37% of the peak (1/e), while calculating the shock-thickness over this period from estimates of MgO U_S and Al/MgO u_P – as determined from hydrocode simulations of the experimental conditions (e.g., Fig. 6A). These simulations also confirm that the Al temperature is ∼constant over the lifetime of the experiment. As thermal conductivity is poorly constrained at our compression conditions, in our hydrocode simulations, we used fixed values determined at ambient pressure conditions.

Calculations of optical-depth along the Hugoniot are also shown from Bolis *et al.* [17] in Fig. 4C. The optical depth is also determined from the shocked-MgO conductivities calculated by Cebulla *et al.* [36] and Soubiran *et al.* [13] using the expression [61],

$$d(E) = \frac{\epsilon_0 c n(E)}{\sigma(E)}, \quad (2)$$

where E is the photon energy (centered around 2 eV for SOP), c is the speed of light, ϵ_0 is the vacuum dielectric permittivity and σ is the calculated shocked MgO electrical conductivity [13, 36]. The refractive index, n, for shocked MgO is estimated through extrapolation of the dependency reported in Ref. [33].

Temperature Determination

The temperature at the shock front is measured with the Omega-EP streaked optical pyrometer (SOP) [21]. The SOP records thermal emission integrated over a 590 to 850-nm spectral range and spatially resolved over the 300-μm field of view (e.g. Fig. 7A). Temperature is calculated assuming gray-body emission where emissivity, ϵ, is defined as ϵ=1-R, where R is sample reflectivity. Temperature as a function of time is given by

$$T(t) = \frac{T_0}{\ln[1 + \frac{(1-R(t))A}{I(t)}]}, \quad (3)$$

where T_0 and A are calibration parameters related to the SOP setup [21], $I(t)$ is the measured intensity of shock-front thermal emission, and $R(t)$ is measured at the 532-nm VISAR wavelength. As T_0 essentially captures the spectral response of the SOP system, and T depends only weakly on this parameter, we assume it is constant: T_0 = 1.909 eV [21, 62]. As potential vignetting through the SOP collection and transport optics can affect the intensity of thermal emission collected, the measured properties of the quartz sample are used as a standard to calibrate the SOP, i.e., to determine the value of A for each shot [57]. The relationship between shock velocity, shock-front temperature and reflectivity in quartz are well known over the pressure range of our experiments [57, 63]. Based on these previous studies we use the following relationships [57]:

$$R_{Qtz} = 4.614 \times 10^{-3} + \frac{(0.3073 - 4.614 \times 10^{-3}) \times U_{S,Qtz}^{9.73}}{U_{S,Qtz}^{9.73} + 16.185^{9.73}}, \quad (4)$$

and

$$T(K) = 1421.9 + 4.3185 \times U_{S,Qtz}^{2.9768}, \quad (5)$$

where R_{Qtz} is the quartz reflectivity as measured at the VISAR probe wavelength of 532-nm. As we measure R_{Qtz} and $U_{S,Qtz}$, this enables us to determine the constant A in Eqn. 3. SOP data for a representative shot are shown in Fig. 7A, where thermal emission from the MgO and quartz layers, and the x-ray probe period are indicated. Also plotted is the calculated shock-front temperature as a function of time (yellow). For each time step, temperature is measured at the shock-front while pressure at the shock-front is calculated from hydrocode simulations (after convergence with measured $U_{S,Qtz}(t)$). During the x-ray probe period, the measured shock-front $T_{MgO}(t)$ is plotted against the calculated shock-front $P_{MgO}(t)$ in Fig. 7B. The values for all shots are listed in Table S1B, and are plotted in Figs. 1A and S1 along with other experimental and theoretical studies.
Uncertainty in temperature: Uncertainties in the determination of temperature include the distribution of temperature states during the x-ray probe period (blue standard deviation error bars in Fig. 7B). Additional systematic uncertainties include uncertainties in the determination of R(t), and uncertainties related to the use of quartz as a temperature calibrant, i.e. the relationship between $U_{S,Qtz}$, R_{Qtz} and T_{Qtz}. We assume that the reflectivity measured at the VISAR 532-nm probe wavelength is representative of the reflectivity over the SOP spectral range of 590-850-nm. We also assume that there are no reflections from the MgO/epoxy/quartz interface. Based on these considerations we estimate an additional systematic uncertainty of ± 300 K for all shots, which is consistent with previous studies [6, 17, 57] (green error bars in Fig. 7B). The temperature uncertainties shown in Figs. 1A and Fig. S1, and listed in Table S1B, represent the combined uncertainties due to the temperature distribution during the X-ray probe period and the systematic uncertainties associated with the temperature measurement.

Density Determination

Diffraction peaks were fit with Gaussian curves to determine peak positions in 2θ, and converted to atomic d-spacing, d = λ /(2 sin θ), where λ is the wavelength of the He_α probe. MgO density, ρ_{MgO}, is calculated individually from the B1 (002), B2 (001) and B2 (011) d-spacing values (Fig. S2). ρ_{MgO} for each shot is listed in Table S1a. We note there is an unexpected low rate of compression as a function of increasing pressure for the B1 and B2 phases (see also Fig. S2). In our analysis we assume the central energy of the X-ray source when calculating d-spacing: 8.368 keV (1.4816 Å). The x-ray source has a ~1% spectral bandwidth [46]. *If* the compressed MgO is a single-crystal, as the d-spacing decreases the Laue diffraction conditions to produce diffraction will only be satisfied by higher photon energies. This effect would potentially result in a slight modification of the inferred d-spacing values, and could also be a contributing factor in the measured reduction of B1 (200) diffraction signal level as as function of pressure (Fig. 1B).

Uncertainty in d-spacing: Reported uncertainty in measured d-spacing includes: (i) accuracy of pinhole reference peaks fit to ideal ambient-pressure 2θ values, (ii) variation in d-spacing as a function of azimuthal angle (ϕ), and (iii) uncertainty in the sample – pinhole (reference plane) distance [47].

Off-Hugoniot states generated by shock unsteadiness: In our experiments, shock unsteadiness in MgO will result in the generation of off-Hugoniot states due to either: (i) isentropic pressure-release from an initial shock state in the case of an unsupported shock, or (ii) shock+ramp-compressed states in the case of a growing shock. For (i) the P-ρ states produced would be less dense than the Hugoniot and for (ii) the P-ρ states produced would be more dense than the Hugoniot. We note that the measured $U_{S,Qtz}$(t) values in our experiments *do* slightly increase over time (by ~1.5-3 %, see Fig. S3B). This may be sufficient to cause a slightly higher compressed state as compared to the shock Hugoniot.

SUPPLEMENTARY MATERIALS

Figure S1. Constraints on the $P-T$ phase diagram of MgO.
Figure S2. Determined pressure-density states of shock compressed MgO [100]
Figure S3. Summary of laser power and shock velocity
Figure S4. X-ray diffraction patterns as a function of pressure.
Figure S5. Equation of state models used for pressure determination.
Figure S6. Pole figure plots for high symmetry B2 planes for Buerger's and WTM mechanisms.
Figure S7. Calculated pole figures for high symmetry B2 planes for WTM mechanism.
Figure S8. Calculated pole figures for high symmetry B2 planes for Buerger's mechanism.
Figure S9. The proposed Buerger's mechanism for the B1→B2 transformation.
Figure S10. Calculated strain needed for the for transformation from B1→B2.
Figure S11. Pressure correction of McWilliams *et al.* shock decay data.
Table S1. Data Summary.

References

[1] M. Mehl, R. Hemley, L. Boyer, Potential-induced breathing model for the elastic moduli and high-pressure behavior of the cubic alkaline-earth oxides. *Phys. Rev. B* **33**, 8685 (1986).

[2] T. S. Duffy, R. J. Hemley, H.-k. Mao, Equation of state and shear strength at multimegabar pressures: Magnesium oxide to 227 GPa. *Phys. Rev. Lett.* **74**, 1371 (1995).

[3] T. Irifune, T. Tsuchiya, *Phase Transitions and Mineralogy of the Lower Mantle, in Treatise on Geophysics (Second Edition)* (Elsevier BV, 2015).

[4] F. Coppari, *et al.*, Implications of the iron oxide phase transition on the interiors of rocky exoplanets. *Nature Geoscience* **14**, 121–126 (2021).

[5] J. Amodeo, *et al.*, Dislocations and plastic deformation in MgO crystals: a review. *Crystals* **8**, 240 (2018).

[6] R. S. McWilliams, *et al.*, Phase transformations and metallization of magnesium oxide at high pressure and temperature. *Science* **338**, 1330–1333 (2012).

[7] F. Coppari, *et al.*, Experimental evidence for a phase transition in magnesium oxide at exoplanet pressures. *Nat. Geosci.* **6**, 926–929 (2013).

[8] S. Root, *et al.*, Shock response and phase transitions of MgO at planetary impact conditions. *Phys. Rev. Lett.* **115**, 198501 (2015).

[9] F. Wagner, N. Tosi, F. Sohl, H. Rauer, T. Spohn, Rocky super-Earth interiors-Structure and internal dynamics of CoRoT-7b and Kepler-10b. *Astron. Astrophys.* **541**, A103 (2012).

[10] S.-i. Karato, Rheological structure of the mantle of a super-Earth: Some insights from mineral physics. *Icarus* **212**, 14–23 (2011).

[11] S. Ritterbex, T. Harada, T. Tsuchiya, Vacancies in MgO at ultrahigh pressure: About mantle rheology of super-Earths. *Icarus* **305**, 350–357 (2018).

[12] J. Bouchet, *et al.*, Ab initio calculations of the B1-B2 phase transition in MgO. *Phys. Rev. B* **99**, 094113 (2019).

[13] F. Soubiran, B. Militzer, Electrical conductivity and magnetic dynamos in magma oceans of Super-Earths. *Nuovo Cimento* **9**, 3883 (2018).

[14] F. Soubiran, B. Militzer, Anharmonicity and phase diagram of magnesium oxide in the megabar regime. *Physical Review Letters* **125**, 175701 (2020).

[15] B. Boates, S. A. Bonev, Demixing instability in dense molten $MgSiO_3$ and the phase diagram of MgO. *Phys. Rev. Lett.* **110**, 135504 (2013).

[16] A. R. Oganov, P. I. Dorogokupets, All-electron and pseudopotential study of MgO: Equation of state, anharmonicity, and stability. *Phys. Rev. B* **67**, 224110 (2003).

[17] R. Bolis, *et al.*, Decaying shock studies of phase transitions in MgO-SiO_2 systems: Implications for the super-Earths' interiors. *Geophys. Res. Lett.* **43**, 9475–9483 (2016).

[18] L. Hansen, *et al.*, Melting of magnesium oxide up to two terapascals using double-shock compression. *Physical Review B* **104**, 014106 (2021).

[19] P. M. Celliers, M. Millot, Imaging velocity interferometer system for any reflector (visar) diagnostics for high energy density sciences. *Review of Scientific Instruments* **94** (2023).

[20] J. R. Rygg, *et al.*, Powder diffraction from solids in the terapascal regime. *Rev. Sci. Instrum.* **83**, 113904 (2012).

[21] M. Gregor, *et al.*, Absolute calibration of the OMEGA streaked optical pyrometer for temperature measurements of compressed materials. *Rev. Sci. Instrum.* **87**, 114903 (2016).

[22] A. B. Belonoshko, S. Arapan, R. Martonak, A. Rosengren, MgO phase diagram from first principles in a wide pressure-temperature range. *Phys. Rev. B* **81**, 054110 (2010).

[23] H. Abu-Farsakh, I. Al-Qasir, A. Qteish, Fundamental properties and phase stability of B1 and B2 phases of MgO over a wide range of pressures and temperatures: A first-principles study. *Comput. Mater. Sci* **154**, 159–168 (2018).

[24] S. P. Lyon, J. D. Johnson, Sesame: the Los Alamos National Laboratory equation of state database. *Los Alamos National Laboratory, Los Alamos, NM, LA-UR-92-3407* (1992).

[25] M. Watanabe, M. Tokonami, N. Morimoto, The transition mechanism between the CsCl-type and NaCl-type structures in CsCl. *Acta Crystallogr. A* **33**, 294–298 (1977).

[26] B. Hyde, M. O'Keeffe, *Phase Transitions, edited by L.E. Cross* (Oxford: Pergamon Press, 1973).

[27] H. T. Stokes, D. M. Hatch, Procedure for obtaining microscopic mechanisms of reconstructive phase transitions in crystalline solids. *Phys. Rev. B* **65**, 144114 (2002).

[28] M. Buerger, *Phase transformations in solids, ch. 6* (New York: Wiley, 1951).

[29] Y. Y. Zhang, *et al.*, Ultrafast x-ray diffraction visualization of $B1$–$B2$ phase transition in KCl under shock compression. *Phys. Rev. Lett.* (2021).

[30] S. D. Jacobsen, *et al.*, Single-crystal synchrotron X-ray diffraction study of wüstite and magnesiowüstite at lower-mantle pressures. *J. Synchrotron Radiat.* **12**, 577-583 (2005).

[31] S. P. Marsh, *LASL Shock Hugoniot Data* (Univ of California Press, 1980).

[32] K. Miyanishi, *et al.*, Laser-shock compression of magnesium oxide in the warm-dense-matter regime. *Phys. Rev. E* **92**, 023103 (2015).

[33] D. E. Fratanduono, J. H. Eggert, M. C. Akin, R. Chau, N. C. Holmes, A novel approach to Hugoniot measurements utilizing transparent crystals. *J. Appl. Phys.* **114**, 043518 (2013).

[34] M. Van Thiel, Compendium of Shock Wave Data. *Lawrence Livermore Laboratory Technical Report, UCRL-50108* pp. 401–405 (1977).

[35] W. Nellis, A. Mitchell, D. Young, Equation-of-state measurements for aluminum, copper, and tantalum in the pressure range 80–440 GPa (0.8–4.4 Mbar). *J. Appl. Phys.* **93**, 304–310 (2003).

[36] D. Cebulla, R. Redmer, Ab initio simulations of MgO under extreme conditions. *Phys. Rev. B* **89**, 134107 (2014).

[37] C. Kwon, Y. Xia, F. Zhou, B. Han, Dominant effect of anharmonicity on the equation of state and thermal conductivity of mgo under extreme conditions. *Physical Review B* **102**, 184309 (2020).

[38] G. Ackland, Elastic properties as a pointer to phase transitions. *RIKEN review* pp. 34–38 (2000).

[39] R. F. Smith, *et al.*, Time-dependence of the alpha to epsilon phase transformation in iron. *J. Appl. Phys.* **114**, 223507 (2013).

[40] B. J. Jensen, G. Gray III, R. S. Hixson, Direct measurements of the α-ϵ transition stress and kinetics for shocked iron. *J. Appl. Phys.* **105**, 103502 (2009).

[41] D. Zahn, S. Leoni, Nucleation and growth in pressure-induced phase transitions from molecular dynamics simulations: Mechanism of the reconstructive transformation of NaCl to the CsCl-type structure. *Phys. Rev. Lett.* **92**, 250201 (2004).

[42] D. Zahn, O. Hochrein, S. Leoni, Multicenter multidomain B1- B2 pressure-induced reconstructive phase transition in potassium fluoride. *Phys. Rev. B* **72**, 094106 (2005).

[43] M. Catti, Ab initio predicted metastable TlI-like phase in the B1 to B2 high-pressure transition of CaO. *Phys. Rev. B* **68**, 100101 (2003).

[44] T. S. Duffy, T. J. Ahrens, Compressional sound velocity, equation of state, and constitutive response of shock-compressed magnesium oxide. *J. Geophys. Res.* **100**, 529–542 (1995).

[45] J. T. Larsen, S. M. Lane, HYADES—A plasma hydrodynamics code for dense plasma studies. *J. Quant. Spectrosc. Ra.* **51**, 179–186 (1994).

[46] F. Coppari, *et al.*, Optimized x-ray sources for x-ray diffraction measurements at the omega laser facility. *Rev. Sci. Instrum.* **90**, 125113 (2019).

[47] J. R. Rygg, *et al.*, X-ray diffraction at the National Ignition Facility. *Rev. Sci. Instrum.* **91**, 043902 (2020).

[48] N. R. Barton, D. E. Boyce, P. R. Dawson, Pole figure inversion using finite elements over rodrigues space. *Textures and Microstructures* **35**, 372532 (2002).

[49] J. V. Bernier, M. P. Miller, D. E. Boyce, A novel optimization-based pole-figure inversion method: comparison with WIMV and maximum entropy methods. *Journal of Applied Crystallography* **39**, 697–713 (2006).

[50] S. Singh, D. E. Boyce, J. V. Bernier, N. R. Barton, Discrete spherical harmonic functions for texture representation and analysis. *Journal of Applied Crystallography* **53**, 1299–1309 (2020).

[51] W. L. Fraser, S. W. Kennedy, The crystal-structural transformation NaCl-type → CsCl-type: analysis by martensite theory. *Acta Crystallogr. A* **30**, 13–22 (1974).

[52] H. D. Bellamy, E. H. Snell, J. Lovelace, M. Pokross, G. E. Borgstahl, The high-mosaicity illusion: revealing the true physical characteristics of macromolecular crystals. *Acta Crystallographica Section D: Biological Crystallography* **56**, 986–995 (2000).

[53] K. Ichiyanagi, *et al.*, Microstructural deformation process of shock-compressed polycrystalline aluminum. *Scientific reports* **9**, 1–8 (2019).

[54] P. M. Celliers, *et al.*, Line-imaging velocimeter for shock diagnostics at the OMEGA laser facility. *Rev. Sci. Instrum.* **75**, 4916–4929 (2004).

[55] A. N. Mostovych, Y. Chan, Reflective probing of the electrical conductivity of hot aluminum in the solid, liquid, and plasma phases. *Phys. Rev. Lett.* **79**, 5094 (1997).

[56] D. Hicks, *et al.*, Shock compression of quartz in the high-pressure fluid regime. *Phys. Plasmas* **12**, 082702 (2005).

[57] M. Millot, *et al.*, Shock compression of stishovite and melting of silica at planetary interior conditions. *Science* **347**, 418–420 (2015).

[58] G. R. Fowles, Shock wave compression of hardened and annealed 2024 aluminum. *J. Appl. Phys.* **32**, 1475–1487 (1961).

[59] R. Hill, *The mathematical theory of plasticity*, vol. 11 (Oxford university press, 1998).

[60] M. Knudson, M. Desjarlais, Adiabatic release measurements in α-quartz between 300 and 1200 GPa: Characterization of α-quartz as a shock standard in the multimegabar regime. *Phys. Rev. B* **88**, 184107 (2013).

[61] M. Millot, *et al.*, Experimental evidence for superionic water ice using shock compression. *Nat. Phys.* **14**, 297 (2018).

[62] S. Brygoo, *et al.*, Analysis of laser shock experiments on precompressed samples using a quartz reference and application to warm dense hydrogen and helium. *Journal of Applied Physics* **118**, 195901 (2015).

[63] D. G. Hicks, *et al.*, Dissociation of liquid silica at high pressures and temperatures. *Phys. Rev. Lett.* **97**, 025502 (2006).

[64] Z. Wu, *et al.*, Pressure-volume-temperature relations in MgO: An ultrahigh pressure-temperature scale for planetary sciences applications. *J. Geophys. Res.* **113** (2008).

[65] R. Musella, S. Mazevet, F. Guyot, Physical properties of MgO at deep planetary conditions. *Phys. Rev. B* **99**, 064110 (2019).

[66] S. Zhang, R. Paul, S. Hu, M. Morales, Toward an accurate equation of state and B1-B2 phase boundary for magnesium oxide up to terapascal pressures and electron-volt temperatures. *Physical Review B* **accepted** (2023).

[67] A. B. Belonoshko, L. S. Dubrovinsky, Molecular dynamics of NaCl (B1 and B2) and MgO (B1) melting: Two-phase simulation. *Am. Mineral.* **81**, 303-316 (1996).

[68] N. De Koker, L. Stixrude, Self-consistent thermodynamic description of silicate liquids, with application to shock melting of MgO periclase and $MgSiO_3$ perovskite. *Geophys. J. Int.* **178**, 162–179 (2009).

[69] A. Zerr, R. Boehler, Constraints on the melting temperature of the lower mantle from high-pressure experiments on MgO and magnesioüstite. *Nature* **371**, 506–508 (1994).

[70] E. Ohtani, Melting temperature distribution and fractionation in the lower mantle. *Phys. Earth Planet. Inter.* **33**, 12–25 (1983).

[71] A. Strachan, T. Çağin, W. A. Goddard III, Phase diagram of MgO from density-functional theory and molecular-dynamics simulations. *Phys. Rev. B* **60**, 15084 (1999).

[72] L. Zhang, Y. Fei, Melting behavior of (Mg, Fe)O solid solutions at high pressure. *Geophys. Res. Lett.* **35**, L13302 (2008).

[73] O. Fat'yanov, P. Asimow, T. Ahrens, Thermodynamically complete equation of state of MgO from true radiative shock temperature measurements on samples preheated to 1850 K. *Phys. Rev. B* **97**, 024106 (2018).

[74] D. Valencia, R. J. O'Connell, D. Sasselov, Internal structure of massive terrestrial planets. *Icarus* **181**, 545–554 (2006).

[75] B. Svendsen, T. J. Ahrens, Shock-induced temperatures of MgO. *Geophys. J. R. astr. Soc.* **91**, 667–691 (1987).

[76] Y. Luo, *et al.*, Equation of state of mgo up to 345 gpa and 8500 k. *Physical Review B* **107**, 134116 (2023).

[77] D. Alfe, *et al.*, Quantum Monte Carlo calculations of the structural properties and the B1-B2 phase transition of MgO. *Phys. Rev. B* **72**, 014114 (2005).

[78] J. K. Wicks, *et al.*, Crystal structure and equation of state of Fe-Si alloys at super-Earth core conditions. *Science Advances* **4**, eaao5864 (2018).

Acknowledgements: We thank the Omega-EP Laser operations staff and the Target Engineering Team at Lawrence Livermore National Laboratory (LLNL) for assistance in these experiments. We thank Paul Asimow for providing the polycrystalline MgO and for useful discussions. We also thank Lowell Miyagi and Joel Bernier, and François Soubiran for helpful discussions. This work was performed under the auspices of the U.S. Department of Energy by Lawrence Livermore National Laboratory under Contract No. DE-AC52-07NA27344. **Funding:** The research was supported by NNSA through the National Laser Users' Facility Program under Contracts No. DE-NA0002154 and No. DE-NA0002720 and the Laboratory Directed Research and Development Program at LLNL (Project No. 15-ERD-012). This work was performed under the auspices of the U.S. Department of Energy by Lawrence Livermore National Laboratory under Contract No. DE-AC52-07NA27344. The research was supported by National Nuclear Security Administration through the National Laser Users' Facility Program (contract nos. DE-NA0002154 and DE-NA0002720) and the Laboratory Directed Research and Development Program at LLNL (project no.'s 15-ERD-014, 17-ERD-014, 20-ERD-044).

Author Contributions: J.W.

and R.S. were responsible for the design and execution of the experiments. D.F. developed the backward characteristics analysis for pressure determination. J.E., M.M and R.R. developed the analysis tools for PXRDIP image processing. J.W., R.S., F.C. and T.D. carried out the experiments. All authors were involved in discussions related to experimental design, data analysis, and interpretation. LLNL AnalyzeVISAR and AnalyzePXRDIP codes were used to analyze the data.

SUPPLEMENTARY MATERIALS

S1. Buerger's mechanism

The Buerger's mechanism [28] is described by a uniform compression of the B1 rhombohedral primitive cell (Fig. S9) in the $[111]_{B1}$ direction and uniform expansion in all directions perpendicular to this. However, this mechanism predicts intensity distribution inconsistent with our measurements. Therefore, it was concluded that this mechanism is not activate. The stretch tensor which map the primitive (rhombohedral) B1 basis vectors, ($\vec{\mathbf{a}}_{\mathrm{P}}, \vec{\mathbf{b}}_{\mathrm{P}}, \vec{\mathbf{c}}_{\mathrm{P}}$) to the B2 basis vectors, ($\mathbf{a}', \mathbf{b}', \mathbf{c}'$) can be determined by calculating the stretches in the principal directions. These directions are the ones along which the deformation is purely hydrostatic. A stretch of 1 preserves the length of vectors in the direction, and any value higher (lower) will expand (contract) vectors in that principal direction.

The Buerger's mechanism requires $\langle 111\rangle_{B1}$ to be one such principal direction. Since there is uniform contraction in the corresponding $\{111\}_{B1}$ plane, any two orthogonal vectors in this plane can be chosen as the other two principal directions. For the example illustrated in Fig. S9, the three principal directions are $\frac{1}{\sqrt{3}}[111]_{B1}$, $\frac{1}{\sqrt{2}}[1\bar{1}0]_{B1}$ and $\frac{1}{\sqrt{6}}[11\bar{2}]_{B1}$. The amount of stretch can be calculated using the XRD measured lattice parameters as shown in Fig. S10A. The direction (S) and stretches (Λ) for shot s22257 (Fig. 2A, 442(28) GPa) are given by:

$$S = \begin{pmatrix} 1/\sqrt{3} & 1/\sqrt{2} & 1/\sqrt{6} \\ 1/\sqrt{3} & -1/\sqrt{2} & 1/\sqrt{6} \\ 1/\sqrt{3} & 0 & -2/\sqrt{6} \end{pmatrix}; \tag{6}$$

$$\Lambda = \begin{pmatrix} 0.6233 & 0 & 0 \\ 0 & 1.2466 & 0 \\ 0 & 0 & 1.2466 \end{pmatrix}.$$

The stretches for the MgO B1→B2 is slightly different than the values reported for NaCl in Ref. [51] (0.6 for the $[111]_{B1}$ and 1.19 for the other two). The stretch tensor is given by $S\Lambda S^{-1}$. This tensor when applied to the rhombohedral B1 basis ($\vec{\mathbf{a}}_{\mathrm{P}} = \frac{\mathrm{a}}{2}[110]_{B1}$, $\vec{\mathbf{b}}_{\mathrm{P}} = \frac{\mathrm{a}}{2}[101]_{B1}$) and $\vec{\mathbf{c}}_{\mathrm{P}} = \frac{\mathrm{a}}{2}[011]_{B1}$ (a is the lattice parameter of the B1 phase), results in the cubic B2 basis vectors ($\mathbf{a}'$, $\mathbf{b}'$, $\mathbf{c}'$ in Fig. S9). These basis vectors in the B1 crystallographic frame are given by $\frac{\mathrm{a}'}{\sqrt{6}}[22\bar{1}]_{B1}$, $\frac{\mathrm{a}'}{\sqrt{6}}[2\bar{1}2]_{B1}$ and $\frac{\mathrm{a}'}{\sqrt{6}}[\bar{1}22]_{B1}$ (a' is the lattice parameter of the B2 phase). There are a total of twelve orientation variants for this transformation mechanism. One such variant ($[\bar{1}11]_{B1}$) is schematically shown in Fig. S9.

S2. Watanabe-Tokonami-Morimoto mechanism

The WTM mechanism, as described in the main text and Fig. 2B, produces a XRD texture pattern consistent with our data. The principal stretches, using the same method described above, depend on the XRD-determined lattice parameters for the B1 and B2 phases. In the WTM mechanism, there is expansion in the $\langle 110\rangle_{B1}$ direction and uniform contraction in the corresponding $\{110\}_{B1}$ plane. The principal direction, S (as columns) and principal stretch, Λ (eigenvalue) along these directions for shot s22257 (Fig. 2A, 442(28) GPa) are given by,

$$S = \begin{pmatrix} -1/\sqrt{2} & 0 & 1/\sqrt{2} \\ 1/\sqrt{2} & 0 & 1/\sqrt{2} \\ 0 & 1 & 0 \end{pmatrix}; \tag{7}$$

$$\Lambda = \begin{pmatrix} 0.8785 & 0 & 0 \\ 0 & 0.8785 & 0 \\ 0 & 0 & 1.2424 \end{pmatrix}. \tag{8}$$

The stretch tensor, F is given by $S\Lambda S^{-1}$. Strain values for all the other shots are presented in Fig. S10B. The WTM mechanism produces six distinct orientation variants.

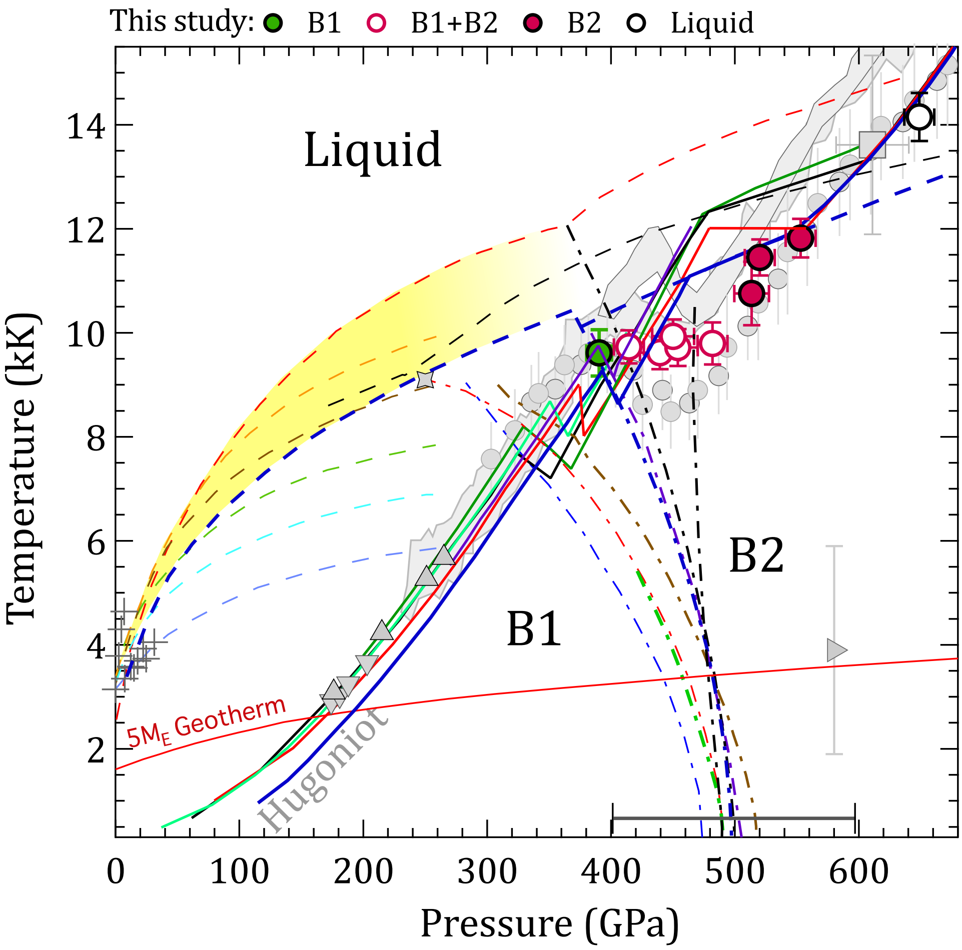

Figure S1. ***P-T*** **phase diagram of MgO.** Plotted are the predicted B1→B2 phase boundary (dashed-dot curves) [8, 12–16, 22, 23, 32, 64–66] and liquid phase boundaries (dashed curves) [8, 13, 15, 67–71] with shaded yellow region constrained at low-pressure by static-compression (gray crosses) [69, 72] and at 250 GPa and 9100 K by gas-gun experiments (gray diamond) [73]. We note there is an additional experimental constraint on the melt curve between 1200-2000 GPa [18]. Also plotted is the estimated onset condition for the B2-phase from laser ramp-compression techniques (gray right-triangle) [7], and an example of the modeled temperature profile within a five-Earth-mass rocky exoplanet (red curve) [74]. Predicted Hugoniots are shown as the solid traces [8, 12–14, 32, 36] and compared to previous *P-T* measurements along the Hugoniot: (gray circles [6] - which have been corrected in pressure based on the subsequent Hugoniot measurements by Root *et al*. [8], see Fig. S11), (gray bands) [17], (gray square) [32], (gray down triangle) [75], (gray up triangle) [76]. The calculated 0-K range of onset pressures for the B1→B2 phase transformation is shown by the scale on the bottom axis (~400-600 GPa) [77]. The data reported in our combined laser-shock compression, X-ray diffraction and pyrometry study are shown as circles (see also Fig. 1a).

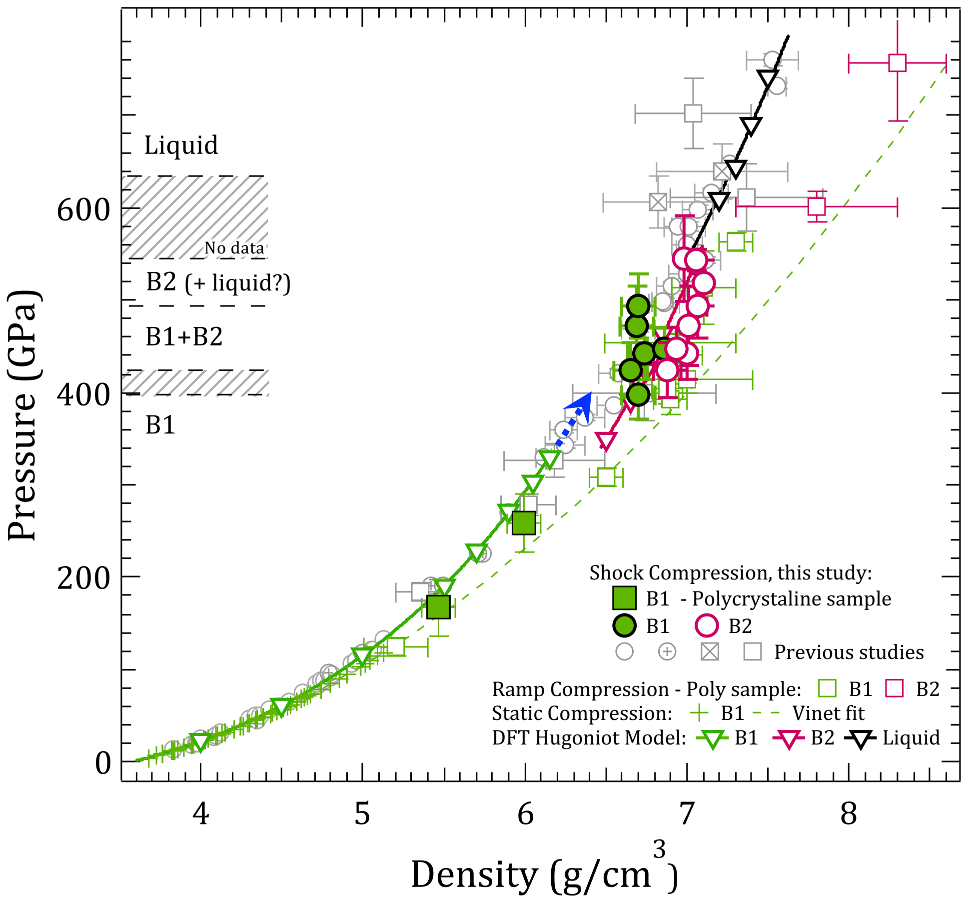

Figure S2. Determined pressure-density states of shock compressed MgO [100]. A summary of published P-ρ data for MgO. Calculated pressure and measured density for the B1 (green filled circles) and B2-phase (maroon open circles). Hugoniot data based on shock-speed measurements are shown as the open gray circle, crossed circle, open square and crossed square symbols [2, 6, 8, 31–34]. A Hugoniot based on DFT calculations is shown as the green (B1), maroon (B2) and black (liquid) open triangles [8]. Solid line fits to these points are based on linear fits in U_s-u_p. The blue dashed arrow represents an extension of the B1 phase up to pressure where we see only B1 in our XRD data. Ramp compression XRD data is shown as open green (B1) and maroon (B2) squares [7], and static compression (B1) data is shown as green crosses [30] with a Vinet EOS fit to high pressure (green dashed). In our experiments, the pressure regions associated with XRD-measured phases are shown by the left axis. The shaded regions represent pressure intervals where no data was obtained. At 425 GPa, measured densities show divergence from previous Hugoniot measurements with increased agreement at higher pressures (~600 GPa) (see also Fig. 3B).

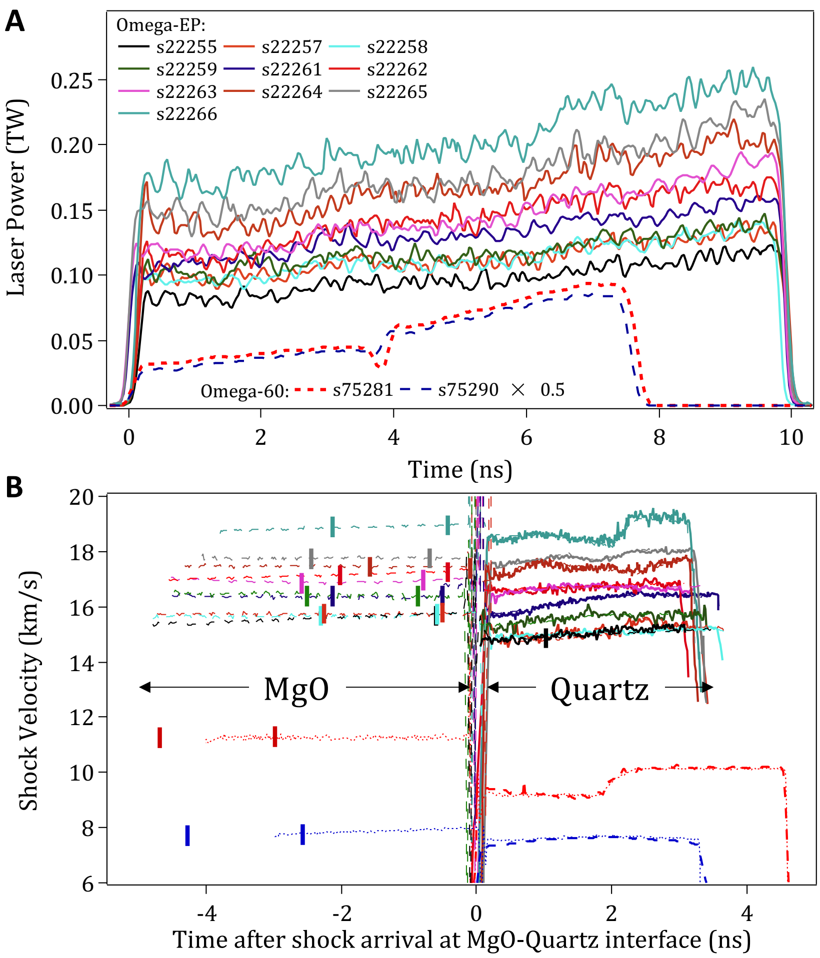

Figure S3. Laser pulse shapes and measured quartz shock velocity profiles for all experiments. (**A**) Laser pulse shapes and (**B**) the associated measured quartz shock velocity, $U_{S,Qtz}$, for all the shots considered in our study (bold solid and bold dashed curves). The light dashed and light dotted curves represent HYADES hydrocode simulations fit to the measured $U_{S,Qtz}$, which provides information on the $U_{S,MgO}$ states during the x-ray probe period (shown here as bound by vertical bars).

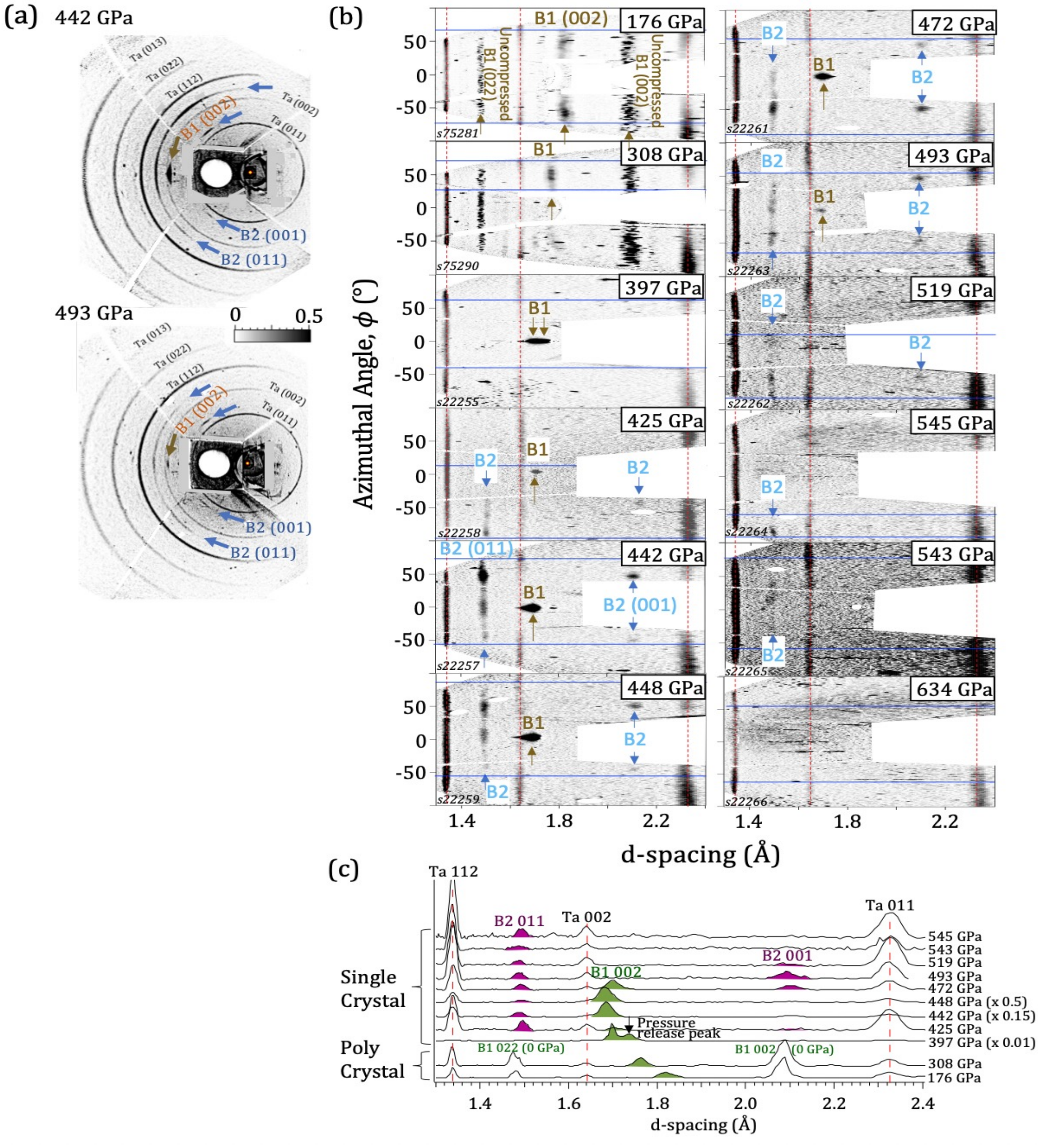

Figure S4. X-ray diffraction data for all shots. **(A)** Stereographic projection of x-ray diffraction data for two representative shots, demonstrating a repeatable texture, and the drop in diffraction intensity, as a function of increasing pressure. Peak photo-stimulated luminescence (PSL) counts for the B1 (002) peak is 145 (top at 442(28) GPa) and 0.8 (bottom at 493(34) GPa). **(B)** Image plates detectors projected as a function of ϕ, and d-spacing for all shots within this study [78]. The red vertical dashed lines represent the positions of the reference peaks from the ambient-pressure Ta pinhole. The textured peaks for the MgO B1- and B2-phase are indicated. For the two lowest pressure shots (176(31) and 308(32) GPa) polycrystalline MgO samples were used. For all other shots single crystal MgO [100] samples were used. **(C)** Lineouts integrated between horizontal blue lines on panels in (b) show Ta reference peaks, B1 and B2 peaks.

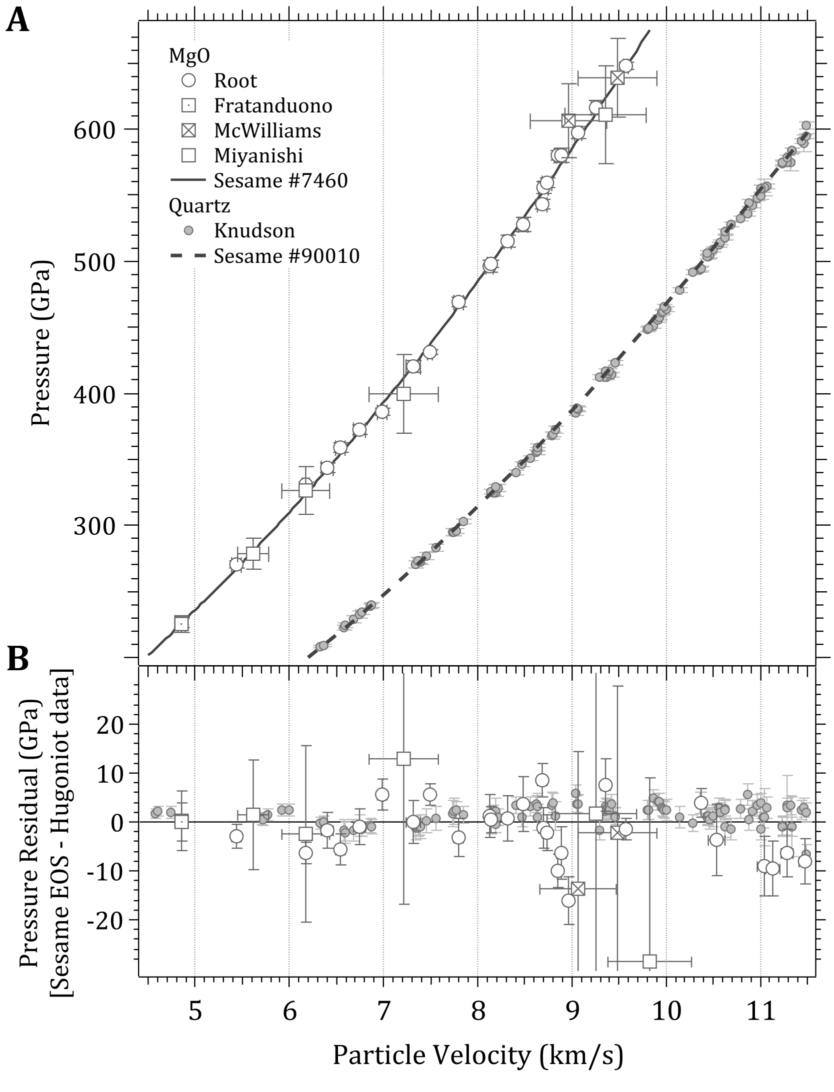

Figure S5. EOS models used in hydrocode calculations. (**A**) Summary of tabulated Hugoniot models used in the hydrocode determination of MgO pressure [24] versus measured Hugoniot density for MgO [2, 6, 8, 31–34] and quartz [60]. **(B)** Pressure residuals of Sesame EOS model Hugoniots – Hugoniot data.

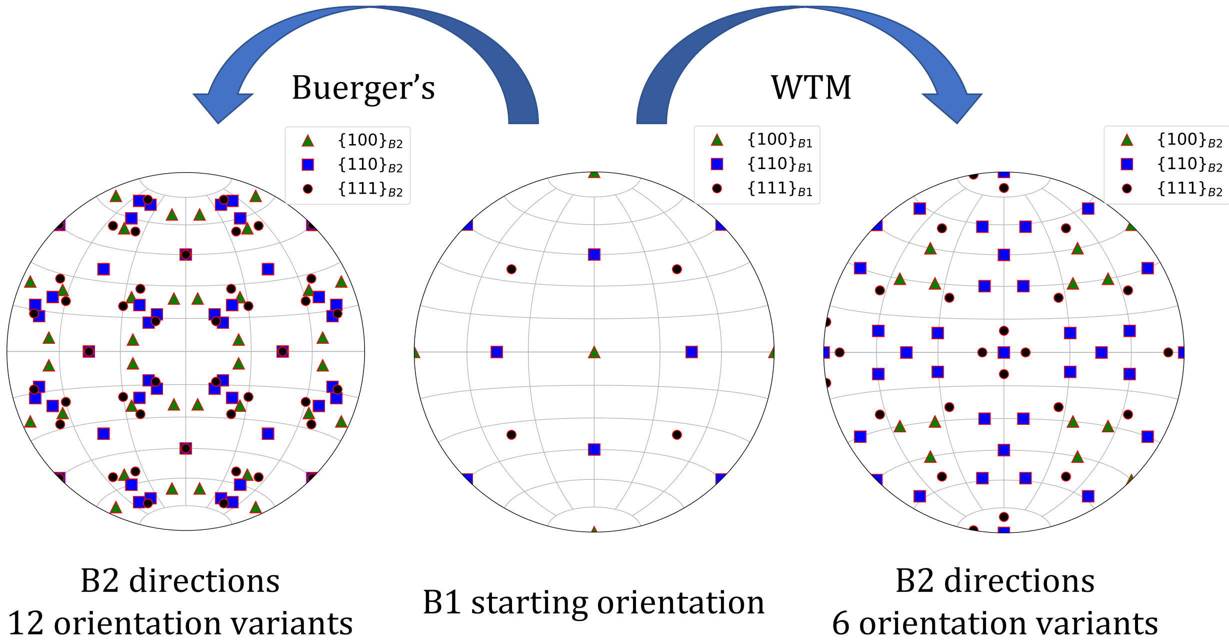

Figure S6. Pole figure.

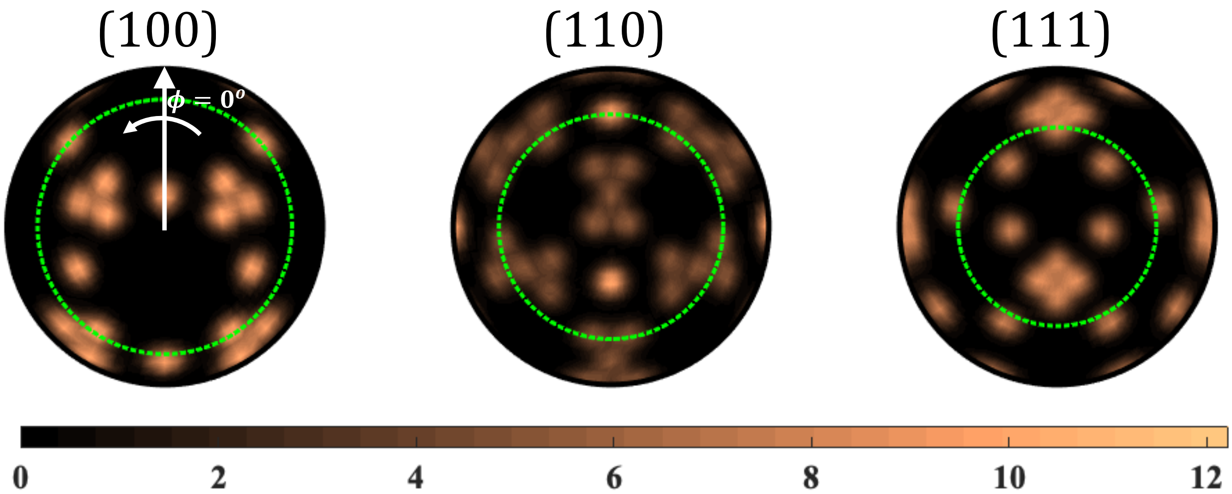

Figure S7. Calculated pole figures for high symmetry planes of the B2 phase as a result of the WTM mechanism. The observable 2θ ring in our experimental geometry is shown by the green circle.

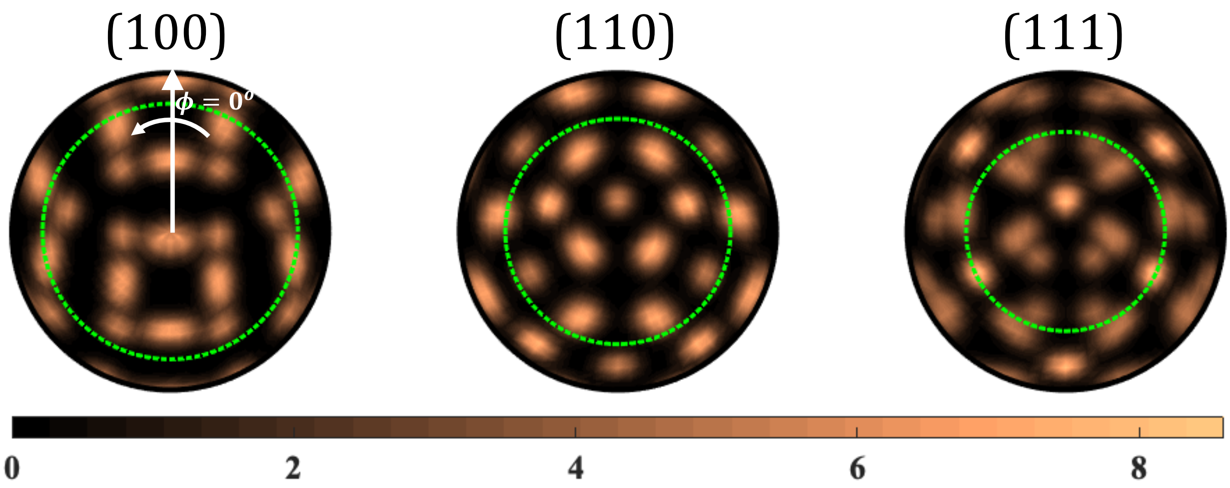

Figure S8. Calculated pole figures for high symmetry planes of the B2 phase as a result of the Buerger's mechanism. The observable 2θ ring in our experimental geometry is shown by the green circle.

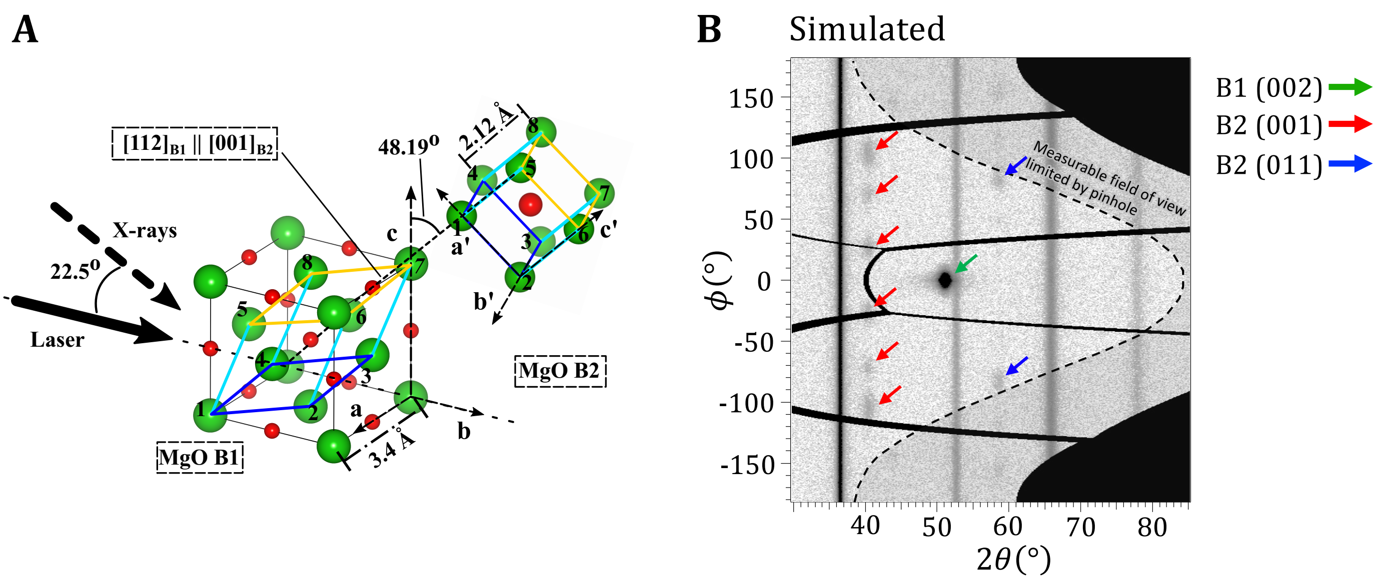

Figure S9. The Buerger's mechanism for the B1→B2 transformation. A. The Buerger's mechanism for the B1→B2 transformation describes compression and rotation of the B1 rhombohedral primitive cell [28] with an orientation relationship of $[112]_{B1}||[001]_{B2}$ and $[1\bar{1}0]_{B1}||[110]_{B2}$. **B.** Using the forward model, for the same grain mosaicity used for simulation Fig. 2A, the resulting diffraction pattern has very different intensity distribution of the B2 phase. Therefore, it was concluded that the Buerger's mechanism is not active.

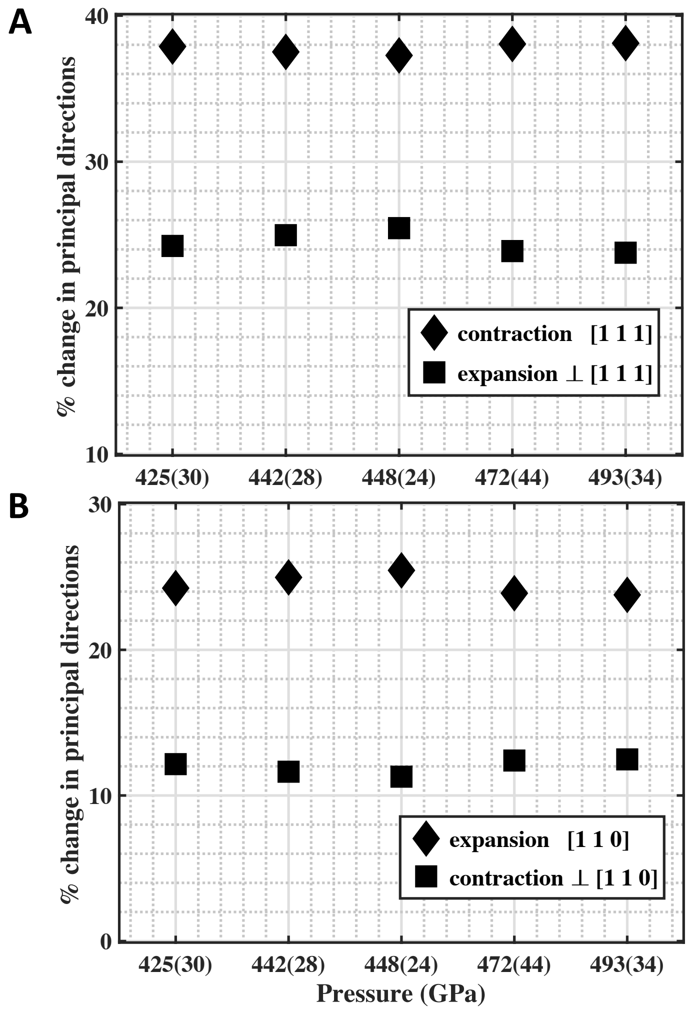

Figure S10. Calculated strain needed for the for transformation from B1→B2. Here, shown for the **(A)** the Buerger's mechanism [28] and **(B)** the ideal WTM mechanism [25]. The pressures for five shots are represented on the x-axis.

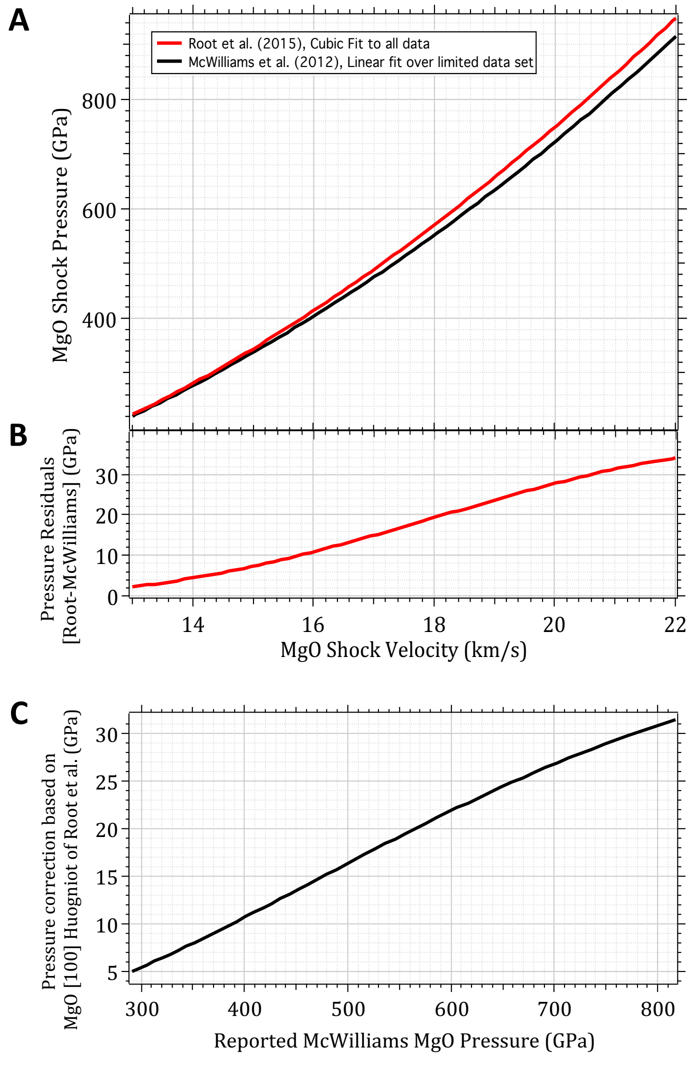

Figure S11. Pressure correction of McWilliams *et al.* shock decay data [6] based on updated MgO [100] Hugoniot data by Root *et al.* [8]. (A) (B) (C).

(A) X-ray Diffraction

P (GPa)	Shot No.	*d*-spacing[a] (Å) B1 (002)	B2 (001)	B2 (011)	Density (g/cm³) B1 (002)	B2 (001)	B2 (011)	B2 Average[#]
176(31)[b]	s75281	1.830	-	-	5.462	-	-	
308(32)[b]	s75290	1.774	-	-	5.995	-	-	
397(26)	s22255	1.709	-	-	6.746	-	-	
425(30)	s22258	1.714(2)	2.141(2)	1.505(2)	6.650(19)	6.817	6.942	6.880(89)
442(28)	s22257	1.707(3)	2.125(3)	1.500(4)	6.734(35)	6.975	7.017	6.996(30)
448(24)	s22259	1.696(7)	2.131(14)	1.505(7)	6.862(80)	6.921	6.941	6.931(14)
472(44)	s22261	1.710(2)	2.121(3)	1.501(2)	6.693(22)	7.016	6.999	7.007(12)
493(34)	s22263	1.710(1)	2.111(4)	1.499(3)	6.702(16)	7.106	7.021	7.063(60)
519(25)	s22262	-	2.109(5)	1.495(8)	-	7.136	7.080	7.108(40)
545(46)	s22264	-	-	1.502 (1)	-	-	6.985	6.985(15)
543(12)	s22265	-	-	1.497(2)	-	-	7.057	7.057(30)
634(29)	s22266	-	-	-	-	-	-	

(B) Pyrometry

P (GPa)	Shot No.	T (K)
-	s75281	-
-	s75290	-
390(10)	s22255	9614(450)
414(12)	s22258	9731(320)
439(16)	s22257	9621(320)
454(16)	s22259	9717(360)
450(17)	s22261	9933(330)
482(12)	s22263	9796(400)
513(14)	s22262	10757(610)
520(12)	s22264	11450(350)
553(12)	s22265	11822(370)
649(12)	s22266	14152(460)

Table S1. **Summary of experimental results. (A)** Measured X-ray diffraction crystal structure and density versus estimated bulk pressure. [a]Uncertainty in d-spacing includes: (i) accuracy of pinhole reference peaks fit to ideal ambient-pressure 2θ values, (ii) variation in d-spacing as a function of azimuthal angle (ϕ), and (iii) uncertainty in the sample - pinhole (reference plane) distance. Pressure uncertainty includes experimental (as determined by the VISAR record) and systematic (uncertainty in material EOS models) contributions. [b]Polycrystalline samples. [#]Values plotted in Fig. 3B. **(B)** Measured average shock-front temperature and calculated average shock-front pressure, during the X-ray probe period. The uncertainties in temperature represent the standard deviation in the measured temperature distribution (see Fig. 7B), combined with an additional ± 300 K estimated to represent systematic uncertainties in the measurement of temperature (see Fig. 1, and Methods and Materials).